NASA Technical Memorandum 86757

NASA-TM-86757 19860000997

Large Eddy Interactions in a Turbulent Channel Flow

S.K. Hong

September 1985

National Aeronautics and
Space Administration

NASA Technical Memorandum 86757

Large Eddy Interactions in a Turbulent Channel Flow

S. K Hong, Ames Research Center, Moffett Field, California

September 1985

National Aeronautics and
Space Administration

Ames Research Center
Moffett Field, California 94035

This Page Intentionally Left Blank

CONTENTS

	Page
SUMMARY	1
INTRODUCTION	1
LARGE EDDIES AND THEIR INTERACTIONS	3
Proper Orthogonal Decomposition Theorem	3
Formulation of Large Eddy Interaction Model	5
Transport Process	7
APPLICATIONS TO CHANNEL FLOW	8
CALCULATION PROCEDURES	11
Initial and Boundary Conditions	11
Mean Velocity Profile	13
Parameter Effects	14
NUMERICAL RESULTS	14
Parameter Determination	14
Eddy-Eddy Interactions	15
Turbulent Stresses	16
Structural Quantities	16
LARGE EDDY STRUCTURE	17
Two-Point Velocity Correlation	17
Typical Velocity Fluctuations	19
Stream Function	20
LARGE EDDY STATISTICS	22
Large Eddy Velocity Field	22
Vorticity Fluctuation	22
Hodograph Transformation	23
Probability Distribution Function	23
TURBULENCE CORRELATIONS	24
CONCLUDING REMARKS	25
APPENDIX A	27
APPENDIX B	29
REFERENCES	32
FIGURES	35

LARGE EDDY INTERACTIONS IN A TURBULENT CHANNEL FLOW

S. K. Hong*

Ames Research Center

SUMMARY

The dynamic processes of large eddies in a turbulent channel flow have been examined by utilizing an orthogonal expansion of the velocity fluctuation, known in the literature as the Proper Orthogonal Decomposition Theorem. The mathematical form of these functions is unknown, in contrast to the Fourier analysis. Attention is focused on the nonlinear, turbulence-turbulence interaction process in the dynamical equation for large eddies (the first term in the expansion). The nonlinear interactions of the components of the first mode are treated exactly, but influences of higher modes are modeled. This requires adjustment of both the skewness and the effective Reynolds number so that the energy equilibrium of the large eddies is ensured when the mean velocity distribution is assumed known from experiments. Computational results show that the first mode contributes significantly to turbulent intensities and possesses a structural and statistical character similar to that of the entire flow.

INTRODUCTION

Important in the engineering predictions of inhomogeneous, turbulent shear flows are the mean velocities and the local structures of turbulence under given initial and boundary conditions. The most popular prediction methods first assume that the Navier-Stokes equations are adequate for describing turbulent flow on an instantaneous basis and then proceed to develop statistical equations for the various turbulent moments, including the Reynolds stresses. However, these equations involve more turbulent moments than equations that exist for them, forming an open system. Various levels of closure schemes have been proposed: the zero-equation model (Cebeci and Smith, 1974), the two-equation model (Saffman, 1970; Jones and Launder, 1972), and the Reynolds stress equation model (Hanjalic and Launder, 1972; Mellor and Herring, 1973). Each of the foregoing methods requires the introduction of several empirical constants with respect to various turbulent processes and provides only approximate predictions of the nature of individual turbulent processes arising in a given flow. An approach that examines the dynamics of the turbulence may require less reliance on modeling. Earlier, the author used the

*NRC Research Associate.

Proper Orthogonal Decomposition Theorem (PODT) (Loeve, 1960; Lumley, 1967) to develop a framework for predicting turbulence structural quantities by modeling nonlinear eddy-eddy interaction terms. At the same time, the framework was used to study the implications of the modeling adopted. The framework, called the Large Eddy Interaction Model (LEIM) (Hong, 1983), is based on the concept that a few properly identified modes in the PODT may be used to represent the technologically important quantities of the turbulent flow field.

It should be noted that Lumley's (1967) primary purpose was to define, unambiguously, the meaning of an "eddy." Given two-point velocity correlations from experiments, the PODT has been applied to pipe flow (Bakewell and Lumley, 1967), a wake (Payne and Lumley, 1967), and a flat plate boundary layer (Lemmerman and Payne, 1977) as a means of extracting the features of a dominant eddy. In a similar approach using the results from a computationally simulated fully developed channel flow, Moin (1984) specifically investigated the number of modes necessary in the PODT to reproduce the turbulent intensities and shear stress. Moin (1984) shows that, in the case of shear stress, it takes the first 15 terms in the PODT representation before the calculated stress distribution matches the value simulated earlier (Moin and Kim, 1982) across the boundary layer. However, when only the wall region is examined, the sum of the first three modes yields the "experimental" results quite well. This small number of modes needed to describe the turbulence gave the author further encouragement to extend the PODT approach, as was done in the LEIM, to be a predictive tool.

The Large Eddy Interaction Model has been applied in the past to variously curved wall boundary layer flows (Hong and Murthy, 1983, 1984a, 1984b). The framework has proved to be useful, among other features, in establishing directly the manner in which (a) anisotropy can arise and change and (b) turbulent transport is affected by the addition or removal of an extra strain in those complex flows. The basic procedure of the LEIM consists of the following steps: (a) decomposing the velocity fluctuations into orthogonal functions with random coefficients, (b) constructing dynamical equations for those functions, (c) identifying the first mode as an organized structure that contributes most to the energy (Lumley, 1967, 1981), and (d) evaluating the large eddy which interacts with the mean flow and the eddy-eddy interactions. However, all the nonlinear terms in the LEIM were modeled in a linear form utilizing either an anisotropic eddy viscosity or a diffusion velocity. In this process, three empirical constants were introduced in the closure and were then determined by matching shapes between normalized Reynolds stresses, calculated from the first mode, and experimental measurements. In view of the emphasis of past applications of the LEIM on evaluating the normalized structure of the first mode, it was primarily a diagnostic method.

In the present work to develop a predictive method, the turbulent transport processes have been re-examined and retained in their nonlinear form. This minimizes the dependence on turbulence modeling and allows evaluation of the magnitudes of the moments. The applicability of the new transport model has been illustrated in a channel flow that is inhomogeneous in the direction normal to the wall. However, the computed results shown here are restricted to the use of only a single

mode in the decomposition. As stated earlier, this forced the introduction of the skewness and the effective Reynolds number as parameters of the problem. Although the current work has not yet demonstrated the uniqueness of a set of these parameters, results based on different sets of these parameters (satisfying the energy equilibrium of large eddies) yield Reynolds stresses that are less than a few percent apart over the entire channel. Structural and statistical properties of the large eddies are then studied from the solution of the first mode. Findings are consistent with the earlier studies on the use of the PODT (that the first mode exhibits the structural nature of the averaged turbulence moments and the statistical nature of the random turbulence). The long term objective is that the LEIM framework be developed further, not only to gain the detailed phenomenological insight into turbulence, but also to provide a means to predict turbulent quantities of engineering interest.

The author appreciates the suggestions provided by Dr. M. W. Rubesin during the course of the work, and his comments on the manuscript.

LARGE EDDIES AND THEIR INTERACTIONS

The mathematical definition of a turbulent eddy as proposed by Lumley (1967), and the method of relating the structure of turbulence to that of a large eddy as developed by Lumley (1967, 1981) and Townsend (1976, 1980), are applied here to turbulent shear flow that is inhomogeneous at least in one spatial direction. A closure assumption is introduced for the nonlinear eddy-eddy interaction term arising in the dynamical equation of the large eddies.

Proper Orthogonal Decomposition Theorem

One can consider a decomposition of the instantaneous velocity, $\tilde{U}_i$, into a mean value and a fluctuation as

$$\tilde{U}_i = U_i + u_i \tag{1}$$

Here we assume that U_i is an ensemble average of $\tilde{U}_i$. Then it is possible to write the velocity fluctuation in terms of orthogonal functions, $\{\phi_i^{(n)}, n = 1,2,3,\ldots\}$. That is,

$$u_i(\vec{x},t) = \sum_{n=1}^{\infty} a_n \phi_i^{(n)}(\vec{x},t)$$

$$\int \phi_i^{(p)} \phi_i^{(q)} \, d\vec{x} \, dt = 0 \qquad (p \neq q;\ i = 1,\ 2,\ \text{or}\ 3) \tag{2}$$

where $\alpha_1, \alpha_2, \alpha_3, \ldots$ are random coefficients with units of velocity and uncorrelated from one another, which means

$$\left.\begin{aligned} \overline{\alpha_n} &= 0 \\ \overline{\alpha_m \alpha_n} &= \lambda^{(n)} \delta_{mn} \end{aligned}\right\} \tag{3}$$

δ_{mn} is the Kronecker delta function defined as

$$\delta_{mn} = \begin{cases} 1 & \text{if } m = n \\ 0 & \text{if } m \neq 0 \end{cases}$$

The overbar, $(\bar{})$, represents the expectation of the event, $(\ )$, in the probability theory and the ensemble average in the turbulence theory. Equation (2) is a generalized Fourier series, accounting for the inhomogeneity of flows by means of discrete functions. It is assumed by definition that $\alpha_1, \alpha_2, \alpha_3, \ldots$ are ordered such that

$$\lambda^{(1)} > \lambda^{(2)} > \lambda^{(3)} > \ldots > 0$$

If one assumes U_1 in eq. (1) to be a time-averaged velocity, one needs a slightly different expansion from eq. (2) as described in appendix A. Equation (3) implies that the coefficients are completely random so that the correlation between the same coefficients is perfect, and between different coefficients is zero. In addition the $\phi_1^{(n)}$'s are assumed to be orthonormal functions, that is

$$\int \phi_1^{(p)} \phi_1^{(q)} \, d\vec{x} \, dt = \delta_{pq} \tag{4}$$

It is noted that the orthonormality condition is imposed only for the u-component functions, and the limits of the integral in eq. (4) are quite arbitrary. The orthogonality condition also implies that none of $\phi_1^{(n)}$'s is identically zero (Tolstov, 1962, p. 41). To calculate the coefficients, α_n, both sides of eq. (2) when $i = 1$ are multiplied by $\phi_1^{(n)}$, and the resulting equation is integrated taking account of the orthonormality condition, eq. (4). The Fourier coefficients are then given by the following form.

$$\alpha_n = \int u(\vec{x},t) \phi_1^{(n)}(\vec{x},t) d\vec{x} \, dt \tag{5}$$

It can be shown, utilizing the randomness in α_n and the orthogonality in $\phi_1^{(n)}$, that $\phi_1^{(n)}$ is related to the two-point velocity correlation, R_{ij}, as

$$R_{ij}(\vec{x},\vec{x}';t,t') \equiv \overline{u_i(\vec{x},t)u_j(\vec{x}',t')}$$

$$= \sum_{n=1}^{\infty} \lambda^{(n)} \phi_i^{(n)}(\vec{x},t)\phi_j^{(n)}(\vec{x}',t') \tag{6}$$

and

$$\int R_{i1}(\vec{x},\vec{x}';t,t')\phi_1^{(n)}(\vec{x}',t')d\vec{x}'\,dt' = \lambda^{(n)}\phi_1^{(n)}(\vec{x},t) \tag{7}$$

where $\phi_1^{(n)}$ are eigenfunctions with $\lambda^{(n)}$ as their eigenvalues of the system. Further, if one considers the integral of the turbulent kinetic energy from the u-component over the whole flow field, then

$$\int \frac{1}{2}\overline{u^2}\,d\vec{x}\,dt = \int \frac{1}{2}\sum_{n=1}^{\infty} \lambda^{(n)}\phi_1^{(n)}\phi_1^{(n)}\,d\vec{x}\,dt$$

$$= \frac{1}{2}\sum_{n=1}^{\infty} \lambda^{(n)} \tag{8}$$

Thus, $\lambda^{(n)}$ represents the kinetic energy content of the entire flow associated with $\phi_1^{(n)}$-mode. The nth mode distributes the energy, $\lambda^{(n)}$, in space and time according to its functional form.

Formulation of Large Eddy Interaction Model

In incompressible turbulent flow, decomposition of the Navier-Stokes equation into the mean and fluctuating parts leads to the following dynamical equation for the velocity fluctuation.

$$\frac{\partial u_i}{\partial t} + U_j\frac{\partial u_i}{\partial x_j} + \frac{\partial U_1}{\partial x_j}u_j + \frac{\partial}{\partial x_j}(u_iu_j - \overline{u_iu_j}) = -\frac{1}{\rho}\frac{\partial p}{\partial x_1} + \nu\frac{\partial^2 u_i}{\partial x_j^2} \tag{9}$$

where p is the pressure fluctuation. Introducing the orthogonal decomposition of the velocity fluctuation, eq. (2), into eq. (9), a dynamical equation is obtained for the eigenmode, $\phi_i^{(n)}$, by the following procedure. First, u_1 is replaced by its expansion; secondly, both sides of the resulting equation are multiplied by a random coefficient, α_m; thirdly, an average is obtained by utilizing the relation, $\overline{\alpha_m\alpha_n} = \lambda^{(n)}\delta_{mn}$; and finally, the remaining equation is divided by $\sqrt{\lambda^{(n)}}$, which leads to the following as first given by Lumley (1967).

$$\frac{\partial \tilde{\phi}_i^{(n)}}{\partial t} + U_j \frac{\partial \tilde{\phi}_i^{(n)}}{\partial x_j} + \frac{\partial U_i}{\partial x_j} \tilde{\phi}_j^{(n)} + \frac{\partial}{\partial x_j} \left\{ \sum_{p=1}^{\infty} \sum_{q=1}^{\infty} \frac{\overline{\alpha_n \alpha_p \alpha_q}}{(\lambda^{(n)} \lambda^{(p)} \lambda^{(q)})^{1/2}} \tilde{\phi}_i^{(p)} \tilde{\phi}_j^{(q)} \right\}$$

$$= \frac{\partial \tilde{\pi}^{(n)}}{\partial x_i} + \nu \frac{\partial^2 \tilde{\phi}_i^{(n)}}{\partial x_j^2} \qquad (n = 1, 2, 3, \ldots) \qquad (10)$$

where

$$\tilde{\pi}^{(n)} \equiv - \frac{1}{\rho} \frac{\overline{\alpha_n p}}{\sqrt{\lambda^{(n)}}}$$

and

$$\tilde{\phi}_i^{(n)} \equiv \overline{\alpha_n u_i} / \sqrt{\lambda^{(n)}}$$

$$= \sqrt{\lambda^{(n)}} \phi_1^{(n)} \qquad (11)$$

$\pi^{(n)}$ is also the nth mode in the series expansion of the pressure fluctuation, that is,

$$- \frac{1}{\rho} p = \alpha_1 \pi^{(1)} + \alpha_2 \pi^{(2)} + \alpha_3 \pi^{(3)} + \ldots$$

It is noted that no constraints are imposed on $\pi^{(n)}$ other than determinacy. Equation (10) thus governs both the shape and intensity of each ϕ_i-mode. The parameter, n, represents the order of modes where it is assumed that the first mode, n = 1, accommodates most of the energy in α_1 and of structure in the dimensionless function, $\phi_1^{(1)}$. Similarly, the second mode, n = 2, is supposed to take up most of what is left, that is, $u_1 - \alpha_1 \phi_i^{(1)}$. The index, i, may have 1, 2, or 3 corresponding to the streamwise direction (x), the local normal to the wall (y), or the spanwise direction (z), respectively. While it is of great interest to solve such a system of equations in general, attention is focused here on the lowest mode for which the dynamical equation becomes the following.

$$\frac{\partial \tilde{\phi}_i^{(1)}}{\partial t} + U_j \frac{\partial \phi_i^{(1)}}{\partial x_j} + \frac{\partial U_i}{\partial x_j} \tilde{\phi}_j^{(1)} + \frac{\partial}{\partial x_j} \left\{ \sum_{p=1}^{\infty} \sum_{q=1}^{\infty} \frac{\overline{\alpha_1 \alpha_p \alpha_q}}{(\lambda^{(1)} \lambda^{(p)} \lambda^{(q)})^{1/2}} \tilde{\phi}_i^{(p)} \tilde{\phi}_j^{(q)} \right\}$$

$$= \frac{\partial \tilde{\pi}^{(1)}}{\partial x_i} + \nu \frac{\partial^2 \tilde{\phi}_i^{(1)}}{\partial x_j^2} \qquad (12)$$

The eddy-eddy interaction term in the above may be said to consist of interactions of large eddy with large eddy, of large eddy with small eddy, and of small eddies with themselves.

For the first eigenmode of pressure fluctuation appearing in eq. (12), one can develop the following Poisson's equation.

$$\frac{\partial^2 \tilde{\pi}^{(1)}}{\partial x_j^2} = 2 \frac{\partial U_j}{\partial x_k} \frac{\partial \tilde{\phi}_k^{(1)}}{\partial x_j} + \frac{\partial^2}{\partial x_k \partial x_j} \left\{ \sum_{p=1}^{\infty} \sum_{q=1}^{\infty} \frac{\overline{\alpha_1 \alpha_p \alpha_q}}{(\lambda^{(1)} \lambda^{(p)} \lambda^{(q)})^{1/2}} \tilde{\phi}_j^{(q)} \tilde{\phi}_k^{(p)} \right\} \tag{13}$$

On the right-hand side of the Poisson's equation are contributions due to interaction between mean velocity gradient and large eddy velocity gradient, and due to interactions among eddies of all sizes. Or, alternatively to eq. (13), continuity relation can be used in the form

$$\frac{\partial \tilde{\phi}_j^{(1)}}{\partial x_j} = 0 \tag{14}$$

Equation (12) with eq. (13) or (14) forms a system of equations for the first mode, $\phi_i^{(1)}$. The nonlinear eddy interaction term in those equations involves higher modes, $\phi_i^{(2)}$, $\phi_i^{(3)}$, $\phi_i^{(4)}$, ... Thus in order to close the system of equations for $\phi_i^{(1)}$, it is necessary either to drop the interactions associated with higher modes or to model the contributions from them.

Transport Process

The nonlinear interaction between the first mode is retained in its original form but the interactions involving modes higher than $\phi_i^{(1)}$ are modeled. A simple way of accounting for the effect of the higher modes is to group them together and to relate this effect to a known quantity. An eddy viscosity is introduced for this purpose (Townsend, 1976, 1980).

$$\sum_{p=1}^{\infty} \sum_{q=1}^{\infty} \frac{\overline{\alpha_1 \alpha_p \alpha_q}}{(\lambda^{(1)} \lambda^{(p)} \lambda^{(q)})^{1/2}} \tilde{\phi}_1^{(p)} \tilde{\phi}_j^{(q)} = \frac{\overline{\alpha_1^3}}{\lambda^{(1)3/2}} \tilde{\phi}_1^{(1)} \tilde{\phi}_j^{(1)} - \nu_T \left(\frac{\partial \tilde{\phi}_1^{(1)}}{\partial x_j} + \frac{\partial \tilde{\phi}_j^{(1)}}{\partial x_1} \right) \tag{15}$$

which has also been suggested by Lumley (1967). In eq. (15), ν_T denotes an eddy viscosity. In the present analysis, ν_T is kept equal to a constant which is independent of mesh dimensions or the distance from the wall. This has an effect of reducing the effective Reynolds number by a factor of $\nu/(\nu + \nu_T)$. Although improved models (with variation in the y-direction) may be required, for simplicity we will use constant ν_T to achieve a steady state solution.

Upon substituting eq. (15) into (12), one obtains a closed system of equations for $\sqrt{\lambda^{(1)}}\phi_1^{(1)}$.

$$\frac{\partial}{\partial t}\tilde{\phi}_i^{(1)} + U_j \frac{\partial}{\partial x_j}\tilde{\phi}_i^{(1)} + \frac{\partial U_i}{\partial x_j}\tilde{\phi}_j^{(1)} + S\frac{\partial}{\partial x_j}(\tilde{\phi}_i^{(1)}\tilde{\phi}_j^{(1)})$$

$$= \frac{\partial}{\partial x_i}\tilde{\pi}^{(1)} + (\nu + \nu_T)\frac{\partial^2\tilde{\phi}_i^{(1)}}{\partial x_j \partial x_j} \qquad (16)$$

where S $(= \overline{\alpha_1^3}/(\overline{\alpha_1^2})^{3/2})$ is the skewness factor of the random coefficient, α_1. Assuming that the mean velocity is given, the system of equations involves then a structural parameter, S, and a stability parameter, ν_T, which need to be chosen. In order for the LEIM to be a completely predictive scheme, it requires incorporation of the mean momentum equation for U_i along with eqs. (14) and (16). For the present, however, emphasis will be placed on how the large eddies interact and react to a known mean flow field.

APPLICATIONS TO CHANNEL FLOW

Fully developed turbulent channel flow has acquired a large data base over the years. Accordingly, two-dimensional channel flow has been chosen to demonstrate the validity of the approximation for nonlinear, eddy-eddy interaction terms, as proposed in eq. (15), and to establish the contribution of the first mode to various statistical turbulence quantities. In the fully developed region of the channel, the mean velocity is one-dimensional. It is dependent only on the normal coordinate, y, where $y = 0$ corresponds to the lower wall and $y = H$ to the upper wall, as shown in figure 1. Thus, the turbulent flow in the two-dimensional channel flow can be regarded as homogeneous in both streamwise (x) and spanwise (z) coordinates, while strong inhomogeneity is retained in the y-direction. For this case, one can define spectral functions for the first mode of velocity fluctuation, $\phi_i^{(1)}$, and of pressure fluctuation, $\pi^{(1)}$, as follows.

$$\hat{\phi}_i(k_1,y,k_3,t) = \frac{1}{(2\pi)^2}\iint_{-\infty}^{\infty}\{\sqrt{\lambda}\phi_i^{(1)}(x,y,z,t)\}\exp\{-\hat{i}(k_1x + k_3z)\}dx\,dz$$

$$\hat{\pi}(k_1,y,k_3,t) = \frac{1}{(2\pi)^2}\iint_{-\infty}^{\infty}\{\sqrt{\lambda}\pi^{(1)}(x,y,z,t)\}\exp\{-\hat{i}(k_1x + k_3z)\}dx\,dz \qquad (17)$$

where k_1 and k_3 are wave numbers and $\hat{i} \equiv \sqrt{-1}$. The superscript indicating mode (1) is omitted in the spectral functions. Applying these definitions into eqs. (14) and (16), one obtains four complex equations with respect to the large eddy spectra, $\hat{\phi}_i$ and $\hat{\pi}$. These equations can be further divided into eight equations for the real and imaginary parts defined according to the following notation.

$$\left.\begin{aligned} \hat{\phi}_1 &= P_1 + \hat{i}P_2 \\ \hat{\phi}_2 &= P_3 + \hat{i}P_4 \\ \hat{\phi}_3 &= P_5 + \hat{i}P_6 \\ \hat{\pi} &= P_7 + \hat{i}P_8 \end{aligned}\right\} \tag{18}$$

The nonlinear terms require the convolution theorem (Lumley and Panofsky, 1964) during the transformation of the system of equations, eqs. (14) and (16), into the mixed, (k_1,y,k_3,t), space. The spectral equations become

$$\frac{\partial\hat{\phi}_1}{\partial t} + \hat{i}k_1U\hat{\phi}_1 + U'\hat{\phi}_2 + S\cdot\mathscr{F}\left\{\frac{\partial}{\partial x_j}(\phi_1^{(1)}\phi_j^{(1)})\right\} - \hat{i}k_1\hat{\pi} - (\nu+\nu_T)(\hat{\phi}_1'' - k^2\hat{\phi}_1) = 0 \tag{19}$$

$$\frac{\partial\hat{\phi}_2}{\partial t} + \hat{i}k_1U\hat{\phi}_2 + S\cdot\mathscr{F}\left\{\frac{\partial}{\partial x_j}(\phi_2^{(1)}\phi_j^{(1)})\right\} - \hat{\pi}' - (\nu+\nu_T)(\hat{\phi}_2'' - k^2\hat{\phi}_2) = 0 \tag{20}$$

$$\frac{\partial\hat{\phi}_3}{\partial t} + \hat{i}k_1U\hat{\phi}_3 + S\cdot\mathscr{F}\left\{\frac{\partial}{\partial x_j}(\phi_3^{(1)}\phi_j^{(1)})\right\} - \hat{i}k_3\hat{\pi} - (\nu+\nu_T)(\hat{\phi}_3'' - k^2\hat{\phi}_3) = 0 \tag{21}$$

$$\hat{i}k_1\hat{\phi}_1 + \hat{\phi}_2' + \hat{i}k_3\hat{\phi}_3 = 0 \tag{22}$$

where $(\,)' \equiv d(\,)/dy$ and $k^2 \equiv k_1^2 + k_3^2$. From equations (19)-(22), we denote

$$\mathscr{F}\left\{\frac{\partial}{\partial x_j}(\phi_i^{(1)}\phi_j^{(1)})\right\} = \iint_{-\infty}^{\infty} \hat{i}k_1''\hat{\phi}_i(\vec{k}'')\hat{\phi}_1(\vec{k}-\vec{k}'') + \frac{d\hat{\phi}_i(\vec{k}'')}{dy}\hat{\phi}_2(\vec{k}-\vec{k}'') + \hat{i}k_3''\hat{\phi}_1(\vec{k}'')\hat{\phi}_3(\vec{k}-\vec{k}'')dk_1''\,dk_3'' \tag{23}$$

where $\vec{k} = (k_1,k_3)$, $\vec{k}'' = (k_1'',k_3'')$, and the double prime, $(\,)''$, when pertaining to the wave number variable denotes a dummy variable for the integration.

From a consideration of two-point velocity correlations and turbulent intensities, a relation can be found between the spectra of the double velocity correlations and the $\hat{\phi}_i$'s as derived in appendix B.

$$\hat{R}_{ij}^{(1)}(k_1'',y,k_3'',t)\delta(\vec{k} + \vec{k}'') = \hat{\phi}_i(k_1,y,k_3,t)\hat{\phi}_j(k_1'',y,k_3'',t) \tag{24}$$

where δ is the Dirac delta function and the superscript (1) indicates the contribution of the dominant mode. $\hat{R}_{ij}$ is defined in

$$R_{ij}(r_1,y,r_3,t) = \iint_{-\infty}^{\infty} \hat{R}_{ij}(k_1,y,k_3,t)\exp\{\hat{i}(k_1r_1 + k_3r_3)\}dk_1\, dk_3 \tag{25}$$

For a flow which is homogeneous in (x,z)-planes,

$$R_{ij}(r_1,y,r_3,t) \equiv \overline{u_i(x,y,z,t)u_j(x + r_1,y,z + r_3,t)}$$

$$= \sum_{n=1}^{\infty} \overline{\alpha_n^2}\phi_i^{(n)}(x,y,z,t)\phi_j^{(n)}(x + r_1,y,z + r_3,t)$$

$$\simeq \overline{\alpha_1^2}\phi_i^{(1)}(x,y,z,t)\phi_j^{(1)}(x + r_1,y,z + r_3,t) \tag{26}$$

where r_1 and r_3 are separation distances and $\simeq$ indicates simple truncation after the first mode. When $r_1 = r_3 = 0$ in eqs. (25) and (26), the two-point correlation reduces to the usual Reynolds stress tensor $\overline{u_iu_j}(y,t)$. Thus, at time t,

$$\overline{u_iu_j}^{(1)}(y,t) = \iint_{-\infty}^{\infty} \hat{\phi}_i(k_1,y,k_3,t)\hat{\phi}_j^*(k_1,y,k_3,t)dk_1\, dk_3 \tag{27}$$

where $(\ )^*$ denotes the complex conjugate of $(\ )$.

The following structural quantities may also be calculated : (a) normal stress intensities $(\overline{u_1^2}/q^2)$, where $q^2 = \overline{u^2} + \overline{v^2} + \overline{w^2}$, (b) shear stress intensity $(\overline{uv}/q^2)$, (c) orientation of the principal axes of the large eddies (θ), which is given by

$$\theta = \frac{1}{2} \tan^{-1}\left(\frac{-2\overline{uv}}{\overline{u^2} - \overline{v^2}}\right) \tag{28}$$

and (d) anisotropy $(\overline{u^2}/\overline{v^2})$.

CALCULATION PROCEDURES

The objective here is to calculate the first mode of the velocity fluctuation and to investigate how much the first mode influences the turbulent intensities and the various other structural quantities described in the foregoing section. Attention is paid to the skewness parameter, S, that appears in eq. (16), and its role in the solution for the first mode, $\phi_i^{(1)}$, and the structure of turbulence deduced therefrom.

In order to solve eqs. (19)-(22), after adopting a numerical algorithm one needs (a) the initial and boundary conditions, (b) the local mean velocity profile, and (c) the proper skewness factor as well as an eddy viscosity. In light of the difficulty in specifying the boundary condition for the pressure spectrum at the wall, the continuity relation is employed in the calculation over the Poisson's equation. Numerical results of the statistical quantities can then be compared with the measurements from Laufer (1951), for example, from which a particular flow condition is selected as

$$U_o = 7.574 \text{ (m/sec)}$$

$$u^* = 0.2891 \text{ (m/sec)}$$

$$H = 12.7 \text{ (cm)}$$

$$Re = U_oH/\nu = 61600$$

where U_o, u^*, H, and Re are the mean velocity at the channel centerline, wall-friction velocity, channel width, and Reynolds number, respectively.

Initial and Boundary Conditions

A numerical solution for the large eddy spectra governed by the system of equations (19)-(22) is determined as an initial-boundary value problem in the (y,t)-space for various values of wave number, $\vec{k}$. The initialization can be approximate because of the implicit nature of the algorithm and the goal of achieving a steady solution in the presence of a fixed mean strain. The initial conditions are chosen to possess reasonable spectral character and spatial distributions. The chosen initial distributions are as follows.

$$\left.\begin{aligned} P_1 &= Ay \exp(-ky) \\ P_2 &= Ay(0.5 - y)/k \\ P_3 &= -P_1 \\ P_4 &= -P_2 \\ P_5 &= A(1 - y)/k/B \\ P_6 &= P_5 \end{aligned}\right\} \tag{29}$$

where A is a constant in the order of 1, and the factor B in P_5 has been introduced so as to make the energy content of $\overline{u^2}$, $\overline{v^2}$, and $\overline{w^2}$, that is,

$$\int_0^1 \overline{u_1^2}\, dy$$

isotropic initially.

At the wall ($y = 0$), the no-slip condition requires

$$P_1 = P_2 = P_3 = P_4 = P_5 = P_6 = 0 \tag{30}$$

The boundary conditions for the pressure spectra (P_7 and P_8) are deduced from the v-component (normal to surface) equation applied at the wall (Moin, Reynolds, and Ferziger, 1978). The spatial derivative for the pressure fluctuation is then discretized using a three-point one-sided formula beginning at $y = 0$.

For the other set of boundary conditions, the flow field has been assumed to be symmetric with respect to the centerline ($y = H/2$), giving

$$P_1' = P_2' = P_5' = P_6' = P_7' = P_8' = 0 \tag{31}$$

$$P_3 = P_4 = 0 \tag{32}$$

where $(\,)'$ denotes the derivative with respect to y. It should be pointed out that the flow field in the entire channel from $y = 0$ to $y = H$ has been solved in a single instance with the no-slip condition imposed at both ends, $y = 0$ and $y = H$. The results show symmetric profiles for the u- and w-spectra, and antisymmetric profiles for the v-spectra (P_3 and P_4) with respect to the channel centerline. This justifies using the current boundary conditions at the centerline.

The semi-implicit numerical scheme employed (Greenspan, 1974) utilizes a two-point backward differencing in time and a three-point central differencing in y. The nonlinear convolution integrals are treated explicitly by evaluating them at a previous time step when the solution is known. The numerical integration for these terms is carried out employing the trapezoidal rule over the wave number space,

(k_1'', k_3''), at a given point, (k_1, y, k_3, t). This enables the formation of a system of matrix equations for all y at each advanced time level, where the coefficient matrix becomes block-tridiagonal and diagonally dominant. The inhomogeneous y coordinate is discretized as suggested by Murphy and Rubesin (1979) and the half of the channel is divided by 35 nonuniform grids.

The wave number space, (k_1, k_3), has also been divided into strongly nonuniform meshes. The wave number plane is covered with (17,17)-grids where the values are equally spaced in the logarithmic scale for each wave number direction in the range between -10 and 10 (1/cm). It was found (from numerical experimentation) that wave numbers outside this range contribute so little energy to the first mode that they have negligible effect on the turbulent stresses.

Mean Velocity Profile

The mean velocity profile is approximated by a near wall Prandtl-Taylor model and a blending profile near the center plane.

$$\text{(a)} \quad U^+ = y^+ \qquad (y^+ < 12)$$

$$\text{(b)} \quad U^+ = 3.0 \ln y^+ + 5.5 \qquad (12 \le y^+ < 760)$$

$$\text{(c)} \quad U/Uo = 1.0 + 0.068 \log(y/d) \qquad (y^+ \ge 760)$$

where $U^+ = U/u^*$, $y^+ = yu^*/\nu$, and $d = H/2$. The mean velocity profile in the outer layer, (c) above, has been introduced in this form for the purpose of matching with the law of the wall, (b) above, smoothly and, of course, with the experimental data.

Parameter Effects

During the computation, a fairly small time step (normalized by the mean velocity at the channel centerline and by the channel height) of about 0.001 has been used to ensure numerical stability and accuracy. Since the current system of spectral equations is nonlinear, an instability in any part of the solutions soon propagates into other solutions. Thus, if solutions for high wave numbers become unstable, even though solutions for low wave numbers are stable, the nonlinear integral causes the entire solution to grow infinitely as the iteration proceeds in time.

Although $\hat{\phi}_i$, governed by eqs. (19)-(22), generally can vary in time, the fully developed, steady mean flow and boundary conditions used here cause the solution to converge to a steady state which represents a stationary random field. We first studied the effect of various values of S on the solution when $\nu_T = 0$. Only a narrow range around the value of zero is found for the skewness parameter, namely $|S| \lesssim 0.03$, for which the solution does not grow rapidly. In the current computation, the procedure has been continued up to 200 iterations in time to achieve an

accurate asymptotic solution. On a Cray operating system, the computation time took 30 sec in the central processing unit for every iteration.

NUMERICAL RESULTS

First, this section will cover how the solution is affected by various values of the parameters, S and ν_T, in eqs. (19)-(22). After a pair of those values is selected, numerical results obtained in the mixed, (k_1,y,k_3,t), space are integrated over the wave number space to yield Reynolds stresses as a function of y. The computed stresses and structural quantities are compared with the experimental data of Laufer (1951).

Parameter Determination

The skewness parameter, S, can be regarded as a parameter affecting the structure of the solution, ϕ. On the other hand, the primary role of the eddy viscosity, ν_T, is to stabilize the growth of the solution, subject to production in a fixed mean velocity field. We pick a value of S first and then determine a corresponding value of ν_T which yields a steady-state solution. One may argue that a choice of a particular set of S and ν_T is not unique on the ground that other combinations of S and ν_T could also produce steady-state results. It has been found, however, that the solution is rather insensitive to the choices of the combinations of S and ν_T that yield steady solutions (see below).

Figure 2 shows the growth of the turbulent kinetic energy, integrated over the channel, for various values of S as a function of time in the absence of higher modes, $\nu_T = 0$, and for a single case with $\nu_T = 18$. With $\nu_T = 0$, the growth rate increases with increasing S, and it was found for $|S| \gtrsim 0.03$ the solution grows so rapidly that it becomes unstable. For $S = 0.01$ and $\nu_T = 18$, however, the desired steady state in kinetic energy is achieved. Also, for $S = 0.03$ a steady solution for kinetic energy occurs when $\nu_T = 22$.

In order to examine further whether each component of the kinetic energy has indeed reached a steady state for the above two sets of parameters, each component of the three turbulent intensities is integrated over the channel from $y = 0$ to $y = d$. The results are presented in figure 3 as a function of time. The results show that the u-component energy for $S = 0.01$ and $\nu_T = 18$ maintains a constant value, but for $S = 0.03$ and $\nu_T = 22$ it continues to decrease slightly. For both cases the w-component continues to increase whereas the v-component decreases, again at a slow rate. The behavior of these different growth rates is believed to be attributed to the use of an isotropic eddy viscosity in eq. (15) and suggests the use of an anisotropic eddy viscosity or some other alternative (Hong and Murthy, 1984a). Nevertheless, in view of the small growth rate in the v- and w-components, this behavior is believed to be relatively unimportant and no attempt was made to eliminate this continually varying anisotropy. The author favors the case of

$S = 0.01$ and $\nu_T = 18$ because it yielded a steady solution, more nearly steady than the other case. However, the calculated Reynolds stresses for these two sets of parameters were well within a few percent of each other as compared in figure 4. Thus, because the choice of which set to use is not critical to the results shown in the rest of the paper, $S = 0.01$ and $\nu_T = 18$ has been used.

Eddy-Eddy Interactions

The eddy-eddy interactions affecting the net production of the first mode will be shown as

$$P(\tilde{\phi}_i^{(1)}) = \underbrace{\frac{\partial U_1}{\partial x_j}\,\tilde{\phi}_j^{(1)}}_{\text{"A"}} + \underbrace{S\,\frac{\partial}{\partial x_j}\,\{\tilde{\phi}_1^{(1)}\tilde{\phi}_j^{(1)}\}}_{\text{"B"}} - \underbrace{\nu_T\,\frac{\partial^2\tilde{\phi}_1^{(1)}}{\partial x_j \partial x_j}}_{\text{"C"}} \tag{33}$$

The term "A" governs interaction with the mean flow. The term "B" corresponds to the transport of the $\phi_1^{(1)}\phi_j^{(1)}$, whereas the term "C" represents the effects of the higher modes modeled by the eddy viscosity. Figures 5 and 6 illustrate the nature of interactions among the eddies which are identified with "B" and "C" in eq. (33). For illustration, the large eddy-large eddy interaction in the P_1-equation (which is the real part of eq. (19)) is used, and is shown in figure 5 for three sets of wave numbers, 0.2, 0.5, and 1.0 (1/cm). It is found that the values of "B" in eq. (33) for wave numbers the same as, or less than, 0.2 (1/cm) are predominantly negative in the inner part of the boundary layer. A negative value of "B" refers to an energy supply; whereas a positive value indicates an energy drain because the value of P_1 itself in the inner layer is negative for those wave numbers. The profiles of the nonlinear term show both types of behavior at the wave number about 0.5 (1/cm) and positive behavior at higher wave numbers than 0.5 (1/cm). Thus the nonlinear eddy-eddy interactions for lower wave numbers cause energy gain, while those for higher wave numbers dissipate the energy.

Shown in figure 6 are comparisons between "B" and "C" terms in eq. (33) for the P_1-equation. Figure 6(a) shows terms "B" and "C" at the low wave number $k_1 = 0.1$ (1/cm) and figure 6(b) compares the same terms at the value of $k_1 = 5.0$ (1/cm), both for a fixed value of the wave number k_3 at 0.05 (1/cm). Profiles of the P_1 are also provided in the two figures to indicate their behavior in y at the same wave numbers. An opposite sign in "B" or "C" from that of P_1 implies energy loss, while the same sign implies an energy gain. The value of $k_3 = 0.05$ (1/cm) was chosen in these illustrations because it emphasizes the differences occurring in the alternative k_1's. Similar results are expected of "B" and "C" for other values of k_3 when k_1 is varied in the same manner. Figure 6(a) shows that at the same wave number ($k_1 = 0.1$) and $y/d = 0.5$ the turbulent energy transfer due to the first mode self-interactions is much smaller than that due to the rest of the modes when the latter are modeled with ν_T = constant. If other models were employed for the eddy-eddy interactions, this emphasis on energy loss might be reduced. The magnitude of the higher-mode interactions considerably

exceeds that of the first mode self-interactions in both figures 6(a) and 6(b) in order to dissipate the energy gained not only from the large eddy but also from the mean flow (term "A" in eq. (33)). Again from the signs of P_1, "B," and "C" in figure 6, one can infer that the higher-mode interactions drain the energy consistently for all wave numbers, while large eddy self-interactions either supply energy for lower wave numbers or remove it for higher wave numbers.

Turbulent Stresses

The real part of the velocity spectrum for the u-component, P_1, and that of the pressure spectrum, P_7, is shown at two different locations of y, which is obtained at time $t = 0.2$. In figures 7 and 8, the P_1- and P_7-spectra are given in the first quadrant of the (k_1,k_3)-space at fixed values of (a) $y^+ = 7$ and (b) $y/d = 0.09$. Generally, one can observe a smooth behavior in the distribution of P_1 and P_7. The value of P_1 in figure 7 is greater at low wave numbers than at high wave numbers, and its distribution falls toward zero with the increasing wave numbers. As the value of y changes from $y^+ = 7$ to $y/d = 0.09$, the lower wave numbers contribute more energy to the P_1-spectrum in the inner layer region than in the viscous dominant region. In figure 8, the P_7-spectrum, unlike P_1, does not change its distribution much as y varies from one position to another. From these deterministic large eddy spectra, P_1 through P_8, Reynolds stress components have been obtained as a function of (y/d) according to eq. (27).

In figures 9-12, the Reynolds stresses obtained as a function of (y,t) are given at every 25 time steps to show the development in time. The solution adjusts itself quickly in time and the effect of the initial conditions appears to be minimal. In order to see whether the Reynolds stresses in figures 9-12 change their profiles, the $\overline{u^2}$- and $\overline{v^2}$-profiles at $t = 0.15$, 0.175, and 0.2 are compared in figure 13 as a function of y/d. It shows that the u- and v-component intensities have indeed achieved equilibrium profiles for $t > 0.15$. The same observation has been made for other Reynolds stress components.

For a detailed comparison, the Reynolds stresses are given as a function of y/d at time $t = 0.2$ in figure 14 along with experimental distributions taken from Laufer (1951). The first mode contributes approximately 30% of the observed intensities, although the shape agrees in general trend with the experimental distribution. The use of isotropic viscosity has caused a spuriously higher proportion of the calculated w-component (than either the u- or v-component) in the contribution to energy.

Structural Quantities

The single-point structural quantities defined in Applications to Channel Flow were calculated from the Reynolds stresses and are compared with corresponding quantities obtained from the measurements of Laufer (1951). In spite of low

intensity levels of the large eddy as shown in figure 14, the normalized structural quantities in figure 15 agree well with the corresponding experimental quantities except for the anisotropy of the flow in the outer part of the boundary layer shown in figure 15(d). It is believed that this latter result is the consequence of the imposed symmetry at the channel centerline, that is, $v = 0$.

LARGE EDDY STRUCTURE

An important quantity in the study of turbulence structure is the two-point velocity correlation which depends on the distance separating the velocities at two different positions. Other useful quantities include the fluctuating velocity vector and stream functions from which a flow pattern may be constructed. We shall present these quantities as deduced from the large eddy computation and discuss their implications in this section.

Two-Point Velocity Correlation

To demonstrate the character of the velocity correlations that can be evaluated from the computation of the first mode, four correlations, R_{11}, R_{22}, R_{33}, and R_{12}, are presented here. The points are separated by r_1, r_2, and r_3 in the x-, y-, and z-directions, respectively, at a fixed time, $t = 0.2$. First, we have calculated correlations between two velocity components which are separated by (r_1 and r_3) in the homogeneous plane (y = constant). Then consideration is given to correlations between velocities separated by r_2 in the y direction.

In figures 16 through 23, the two-point velocity correlations (obtained from eq. (25) and normalized by the maximum value at each y location) are shown at two planes across the channel, namely $y^+ = 7$ and $y/d = 0.5$, as a function of separation distance (r_1, r_3). At $y^+ = 7$ in the viscous sublayer the correlations fall off rapidly to a zero value, but oscillate thereafter as the separation distance increases in both x- and z-directions. A negative region in the correlation surface indicates that the velocity fluctuation in that region is generally opposite from the one at the origin. Thus, the distance between the two adjacent peaks in figures 16-19 reflects a macro-length scale of motion in the region. On the other hand, the correlations at $y/d = 0.5$ drops slowly over the distance of approximately a channel half-width. In general, one can infer that the normal velocities, v, have shorter correlation lengths than the other velocity components. When the correlations in figures 16-23 are compared with the ones observed experimentally (Comte-Bellot, 1963), the distance for which the correlation changes its sign or reaches its minimum is longer in the current calculations than in the measurements. In general, these correlations exhibit the different character among the components in R_{ij} and between different locations in y. For example, the longitudinal correlation, R_{11} in figure 20, and the lateral correlation, R_{22} in figure 21, display the typical behavior of these quantities; that is, the R_{11} asymptotes to a zero value while the R_{22} crosses the zero line in a short distance and comes back

to $R_{22} = 0$. But all correlations are symmetric with respect to r_1 and r_3 for all y's, which is consistent with the homogeneity assumption of the flow in the (x,z)-plane.

An interesting way of examining the correlation coefficients is to introduce a length scale, ℓ_i, deducible from the correlations in the form

$$\ell_1^2(y) = \int_0^\infty \int_0^\infty R_{ii}(r_1,y,r_3)dr_1\, dr_3 \tag{34}$$

Here the subscript, i, may be 1, 2, or 3 corresponding to the x-, y-, or z-coordinates, respectively. The length scales obtained from eq. (34) for different "i" are compared across the channel in figure 24. One observes the distinct anisotropy in the length scales among the directional components. Also the magnitude of the length scales is on the order of the channel half-width, d, with the largest x-component and the least y-component scales. The length scales defined this way represent the size of the large eddy (Townsend, 1976, p. 50) along y, where the size in the ith direction is proportional to each component of the length scale, ℓ_i.

Next, normal correlations of the velocities are examined as a function of (y,r_2) in the form

$$R_{1i}(y,r_2) = \frac{\overline{u_i(y)u_1(y + r_2)}}{\{\overline{u_1^2}\}_{max}} \tag{35}$$

In the calculation, the R_{1i} are evaluated at $t = 0.2$ for every (x,z)-point in a range which covers about two periods in each of the x- and z-directions. Then the correlations are averaged over the (x,z)-plane. Such correlations are shown at two values of y in figures 25 and 26. At $y^+ = 7$ in figure 25, the u- and v-correlations approach asymptotically a near zero value within a distance of about 0.1d, whereas the w-correlation drops to a zero value within 0.05d. On the other hand, the correlations at $y/d = 0.5$ decrease mildly with increasing separation distance as shown in figure 26. The shapes of the three correlations in figure 26 are also very similar to one another except in the region very close to the wall. The anisotropy among the three correlations is more severe at $y^+ = 7$ than at $y/d = 0.5$, but the correlation is weaker in the viscous region than in the outer layer. It means that the velocities are more likely to be in the opposite sign in the viscous region than in the outer layer.

Again length scales are assigned to the correlation coefficients defined in eq. (35) in the following form.

$$L_i(y) = \int_{-\infty}^{\infty} R_{1i}(y,r_2)dr_2 \tag{36}$$

The length scales, L_i, then represent the degree of mixing of the fluid in the y direction associated with each velocity component. Figure 27 shows the length scales obtained from eq. (36) as a function of y/d. On the same figure, a mixing length scale deduced from

$$\overline{uv} = -\rho \ell_m^2 \left(\frac{\partial U}{\partial y}\right)^2 \tag{37}$$

is provided for a qualitative comparison between L_1 and ℓ_m and is denoted by points (•). The values of the scale, ℓ_m, are taken from Goldstein (1950, p. 357) for a pipe flow at the same Reynolds number as in the current channel flow. Thus the length scales, L_i, are comparable to the conventional mixing length scale in magnitude as well as in distribution. But, as can be observed in figure 27, the x-component length scale, L_i, becomes locally negative in the viscous region. This is perhaps because the effect of small-scale turbulence is excluded in that region where the influence of small eddies is comparable to that of large eddies.

As an alternative to the integral scale, L_i, as defined in eq. (36), one can define a length scale as the distance for which the correlation crosses a zero line. The slope of such a length scale may be found to be steeper (Glushko, 1965) than the current slope of about 0.4 in the inner region (y/d < 0.2) in figure 27.

Typical Velocity Fluctuations

Characteristics of the turbulent velocity field can be displayed, in the ensemble-averaged sense, from the first mode. If one writes a typical velocity field corresponding only to the first mode as $u_1^{(1)}$, then $u_i^{(1)}$ may be obtained from

$$u_i^{(1)}(x,y,z,t) = \sqrt{\lambda^{(1)}}\phi_1^{(1)}(x,y,z,t)$$

$$= \iint_{-\infty}^{\infty} \hat{\phi}_1(k_1,y,k_3,t)\exp\{\hat{i}(k_1x + k_3z)\}dk_1\, dk_3 \tag{38}$$

Contour plots of the typical velocity fluctuations can then be drawn in a physical domain between -0.5H and 0.5H for both x- and z-coordinates. To show the turbulent motion in the near wall region, the contour plots of the three velocity components, $u^{(1)}$, $v^{(1)}$, and $w^{(1)}$, are presented at $y^+ = 7$ in figures 28-30. In the figures, solid lines indicate positive values and dashed lines indicate negative velocities. The inner curves possess higher values than outer curves enclosing them, and the increment between contour curves is uniform throughout the figures. The solid and dashed lines appear alternatively in both x- and z-directions showing a periodic occurrence of the "thumbprints." The contour curves are more circular than similar

results from the direct simulation of the flow (Moin and Kim, 1982) where the contour lines form elongated curves in the streamwise direction. The contour plots exhibit periodic formations in both directions and the spatial periodicity is shown to be one-half of the channel height (H/2), although there are also weak secondary periods within the principal period. This is a consequence of the Fourier transform utilized in the calculation procedure. One advantage of the spectral method over the finite difference method is that the latter requires a period length in the homogeneous directions when imposing the boundary conditions while the former does not need it. The magnitude of the period in the spectral method is determined implicitly as a function of the large eddy spectral content and is dependent on the nature of turbulence rather than artificial geometry. Since the flow domain in the figures covers two periodic lengths in both directions, it is considered adequate in studying any feature deduced from the region as a typical property of the flow as a whole.

Stream Function

The velocity vector of the first mode is plotted in figure 31 in the (y,z)-plane at two values of x, that is, x/H = 0.3 and 0.4. The choice of 0.3 and 0.4 is not significant since the turbulent motion is shown to be periodic and repetitive in the previous section. The two locations are chosen simply because they seem to possess some character of the flow. The flow at 0.3 and 0.4 appears to be chaotic in figure 31. In order to grasp the flow field associated with the velocity vectors, a stream function, ψ_1, is defined in the (y,z)-plane as follows.

$$\psi_1(x,y,z) = -\int_0^y w^{(1)}(x,y,z)dy \tag{39}$$

The stream function, ψ_1, represents the turbulent flux of mass between the surface and a point in space. A positive value implies the bulk of the flow moving in the negative z-direction and a negative value implies movement in the positive y-direction. The contours of the stream function are drawn in figure 32 and, in a three-dimensional format, in figure 33, where the geometrical extent of the flow field in the (y,z)-plant is the same as in figure 31. The solid lines bear positive values, and the dashed lines correspond to negative stream functions. Figure 32 shows contour curves of ψ_1 obtained at (a) x/H = 0.3 and (b) 0.34. The stream function contours when chosen at 0.3 and 0.34, instead of 0.3 and 0.4, reveal clearly the turbulent motion in the spanwise direction as well as that in the streamwise direction. First, the bulk motions of turbulent flow push each other in the spanwise direction, resulting in a counter-rotating flow. The centers of each bulk motion are located at the regions of highest contour values in figure 32. Secondly, the line connecting points A-E in figure 32 rises to the line A'-E' in the adjacent downstream plane. The values of the stream function remain unchanged as the flow moves from A to A', and B to B', etc. The streamlines connecting the two lines are elevated by approximately 0.06 in y/H between 0.3 and 0.34 in x/H.

Thus one can estimate that the large eddy structure is inclined with respect to free-streamline by an angle of arctan(0.06/0.04) = 56 (degrees).

In figure 33, the levels of the stream function contours remain unchanged as the x/H progresses from 0.3 to 0.5. The streamlines at x/H = 0.5 have been added primarily to show the periodic nature of the motion in the homogeneous direction. The main feature in figure 33 is the lifting of the streamlines as the flow moves on from x/H = 0.3 to 0.4. If one compares figure 31 with 33, the flow in the inner region (y/d < 0.3) at x/H = 0.3 is more energetic than at x/H = 0.4. This is because the flow has gushed up toward the outer region by a movement of counter-rotating vortices at x/H = 0.3 and as a result has lost its energy by the time it reaches x/H = 0.4. The lower portion of the flow field in figure 31 is indeed very quiet and represents a very weak motion. After resting briefly at around x/H = 0.4, the flow is then ready again for another leap at around x/H = 0.5.

When attention is focused on the streamlines in the viscous region, as in figure 34 where physically the spanwise extent is six times the vertical extent, two opposing streamline patterns emerge. The distance between the centers of the dominant motions is about 140 wall units (normalized by the wall-friction velocity and the molecular viscosity). This is higher than the 50 wall units estimated by Blackwelder and Eckelmann (1979) for the spanwise distance between a pair of counter-rotating streamwise vortices. Nevertheless, the ψ_1 shown on figure 34 again demonstrates the existence of a counter-rotating vortex motion which intrudes the viscous layer. These are the same motions which have been advocated by Bakewell and Lumley (1967) and by Moin (1984).

In addition to the previously defined stream function, ψ_1, in the (y,z)-plane, a second stream function, ψ_2, may be considered in the (x,y)-plane to attempt to explain the manner in which the large eddy behaves in the streamwise direction. Now, if the second stream function, ψ_2, is expressed in the form

$$\psi_2(x,y,z) = \int_0^y u^{(1)}(x,y,z)dy \tag{40}$$

then the ψ_2 describes the flux of the turbulent flow in the streamwise direction across a vertical line from the wall (y = 0) to a point of interest (y). The curves pushed toward the positive y-direction imply that the flux of turbulent flow is going into the positive x-direction, while the curves dipped toward the bottom wall indicate that the turbulent flow is returning back against the mean flow even though the total velocity is still positive. In figure 35, if one examines the flow region between x/H = 0.3 and x/H = 0.4 only, the streamlines bounded by the first two (x,y)-planes from the low z values are indented toward the bottom. On the contrary, the streamlines surrounded by the last two (x,y)-planes show the opposite. One can infer, therefore, that the motion of the large eddies pushes the fluid forward, stagnates, and then pulls it backward, forming a shape analogous to a horseshoe or hairpin (Willmarth and Tu, 1967). However, the structure inferred from figures 33 and 35 covers a greater spatial extent than the one suggested, for

example, by Hinze (1975), and virtually the whole flow field becomes affected where such structure arises. The structure occurs sporadically in space, with a principal period equaling the channel half-width in the homogeneous directions. Within the principal period smaller, sub-harmonic motions are also observed.

LARGE EDDY STATISTICS

While correlation functions, vector plots, or stream functions of the first mode reveal an essential nature of the turbulenty motion, another side of turbulence can be exposed by vorticity fluctuations and probability functions. To enhance our understanding of the large eddies, we further investigate the velocity fluctuations from different points of view and their respective statistical properties. We shall briefly examine the hodograph transformation of the large eddy velocity components.

Large Eddy Velocity Field

The same velocity fluctuations, obtained from eq. (38) and discussed in Typical Velocity Fluctuations, are then displayed in the (y,z)-plane mainly to show their variations in the inhomogeneous space, y, for successive locations of z. Most fluctuations are concentrated in the wall region as shown in figures 36-38 where the energy production is large. One notable feature is how the fluctuation at the wall is related to the outer edge of the boundary layer, which is reminiscent of the ejection or inrush (Hinze, 1975, p. 666). The ridges in figure 37 may be identified with the ejection originating at the top of each hill, and the valleys can be related to the inrush. The two phenomena occur intermittently in the horizontal (x,z)-plane but are connected throughout the y-direction. This shows that the turbulent transport transmits most of the energy or the momentum through the transmittal routes in the normal direction.

Vorticity Fluctuation

Although an eddy is a different concept from a vortex, efforts have been made to trace the eddy from the dynamics of the vortex motion. The vorticity is further distinguished from the vortex but can be indicative of turbulent motion, especially through the formation of a vortex tube. The streamwise component of the vorticity fluctuation is calculated from the large eddy and is shown in figure 39. For qualitative study, however, the differentiation of the velocity is performed in the physical space using a central differencing. If one wishes higher accuracy, one can differentiate the velocity spectrum analytically and then integrate it over the wave number space. The streamwise vorticity reveals highly concentrated counter-rotating vortices along the spanwise direction. The vorticity in the outer layer is surprisingly quiet in contrast to the energetic velocity fluctuations in that region.

Hodograph Transformation

With the anticipation that the hodograph transformation may hold a clue for the description of the large eddies, the velocity flow field of the first mode in a finite domain in the physical space has been transformed into the so-called hodograph-(u,v,w)-space. A flow volume taken from the (x,y,z)-space at a fixed time, $\tilde{t} = 0.2$, as shown in figure 40, is represented by 35 grid points along each of 36 lines sampled. Velocity components at each grid point along the vertical lines are then mapped into the hodograph space, as shown in figure 41, and the points are connected in the direction of the arrows. The result is 36 tangled lines in the (u,v,w)-space, forming a finite region in the new space. Each trajectory in the hodograph space consists mostly of loops with relatively large radii of curvature. As noted by Deissler (1984) in the description of a flow with all sizes of eddies transformed into a phase space, the trajectory for the small-scale turbulence might have included loops with smaller radii of curvature than the ones shown in figure 41. It is also noticeable that there are no cusps in the trajectories due to inherent large scales associated with the first mode. In the figure, all the paths are heavily concentrated around the zero-velocity point, and the trajectories follow the curve, $u = -v$, when projected on the (u,v)-plane as shown in figure 42.

By the same way, streamlines passing through the (x,y)-plane at $z = 0$ are projected into the hodograph space. The grid points from which velocities are taken are shown in figure 43, and the velocities are then mapped into the hodograph space in figure 44. The transformed shape in figure 44 is obtained after connecting all the points in both x- and y-directions. The trajectories again show very much the same shape as found earlier in figure 41 from another volume of flow. It is evident from the two figures that any streamlines in the turbulent channel flow, when converted into the hodograph space, would lie on the surface enclosed by the 36 arrowed lines in figure 41. Thus the large eddy velocity components in the channel flow form an ellipsoid in the (u,v,w)-space whose major axis is aligned with a diagonal represented by $u = -v = w$. This is consistent with the proposed description of a large eddy by Townsend (1956) and other experimental observations in which correlations between u and v, for example, are most likely negative leading to negative shear stress.

Probability Distribution Function

In previous hodograph figures as well as velocity contour plots, it is apparent that the velocity fluctuations pass through the zero point ($u = v = w = 0$) more often than any other points. When 2601 ($= 51 \times 51$) grid points were sampled in an (x,z)-plane at $y^+ = 7$ or $y/d = 0.5$, the number of points at which the velocity falls into a certain threshold between maximum and minimum velocities shows a typical near-Gaussian distribution as in figure 45. The distribution in the homogeneous plane slightly deviates from the Gaussian and the degree of departure from it indicates the degree of skewness of turbulence. The skewness is believed to be a result of the nonlinear transport term in eq. (16) which was necessary for the energy balance of the large eddies. In figure 45, two propability distribution function

(PDF) curves are presented for two different locations of y, and the skewness changes its sign as y increases. This agrees with experimental trends (Kreplin and Eckelmann, 1979). When the u-component velocity is sampled along a vertical line in y at two locations of (x,z) = (0,0) and (0.1,0.1) as illustrated in figure 46, the resulting PDF is not even close to a Gaussian distribution, thereby confirming that the PDF in the inhomogeneous space is not normal as expected.

The statistical results discussed in this section are obtained from the first mode; nonetheless they disclose salient features of the entire turbulent motion for a given flow, either experimentally observed or derived from analysis. It is thus certain that the first mode retains most of structural and statistical information embedded in an actual flow.

TURBULENCE CORRELATIONS

The nature of the orthogonal decomposition of the velocity fluctuation into random and deterministic variables in the Large Eddy Interaction Model could enable one to calculate various turbulent correlations directly from the solution of $\phi_1^{(n)}$ and $\pi^{(n)}$. As an illustration, we now consider two important processes appearing in the Reynolds stress equations; that is, the pressure-strain rate correlation, π_{ij}, and the rate of dissipation of the turbulent kinetic energy, ϵ_{ij}, where

$$\pi_{ij} \equiv \overline{\frac{p}{\rho}\left(\frac{\partial u_i}{\partial x_j} + \frac{\partial u_j}{\partial x_i}\right)} \tag{41}$$

$$\epsilon_{ij} \equiv 2\nu \overline{\left(\frac{\partial u_i}{\partial x_k}\,\frac{\partial u_j}{\partial x_k}\right)} \qquad \text{(sum for index } k\text{)} \tag{42}$$

We recall the expansion in the form

$$u_i = \alpha_1\phi_i^{(1)} + \alpha_2\phi_i^{(2)} + \alpha_3\phi_i^{(3)} + \ldots \tag{43}$$

$$-\frac{1}{\rho}\,p = \alpha_1\pi^{(1)} + \alpha_2\pi^{(2)} + \alpha_3\pi^{(3)} + \ldots \tag{44}$$

where $\pi^{(n)}$, $n = 1, 2, 3, \ldots$, are the solutions of the coupled dynamical equations governing $\phi_i^{(n)}$ and $\pi^{(n)}$ (see eqs. (10) and (13)), but are not necessarily mutually orthogonal.

Due to the randomness in the α_n's, one can express π_{ij} and ε_{ij} in the form

$$\pi_{ij} = [\overline{\alpha_1^2}(1)S_{ij}^{(1)} + \overline{\alpha_2^2}(2)S_{ij}^{(2)} + \ldots]$$

$$= -\sum_{n=1}^{\infty} (\sqrt{\lambda^{(n)}}\pi(n))(\sqrt{\lambda^{(n)}}S_{ij}^{(n)}) \tag{45}$$

$$\varepsilon_{ij} = 2\nu \sum_{n=1}^{\infty} \left(\frac{\partial\sqrt{\lambda^{(n)}}\phi_i(n)}{\partial x_k}\right)\left(\frac{\partial\sqrt{\lambda^{(n)}}\phi_j(n)}{\partial x_k}\right) \tag{46}$$

where

$$S_{ij}^{(n)} \equiv \frac{\partial\phi_i^{(n)}}{\partial x_j} + \frac{\partial\phi_j^{(n)}}{\partial x_i}$$

Concurrently with the homogeneity assumption in the channel flow case, π_{ij} and ε_{ij} can also be expressed as a function of spectra, $\hat{\phi}_i$ and $\hat{\pi}$, as well (Hong and Murthy, 1984b).

Therefore the Large Eddy Interaction Model can be utilized as a guide to test and to aid in closing various turbulence models.

CONCLUDING REMARKS

The current paper deals only with the first mode and the balance of a large eddy regarding its origin, maintenance, and destruction . Therefore, the question still remains untouched as to the number of modes in the series required to represent the turbulence field sufficiently well to predict engineering quantities. The first mode is shown, however, to be so significant that it supplies about 30% turbulent kinetic energy and possesses a structural and statistical character that matches well with the experimental trends of the entire turbulence field.

When the turbulent transport is truncated to only the interactions between the components of the first mode ($\nu_T = 0$), it is found that the energy drain through the first mode is insufficient to balance the energy gain from the mean motion. The kinetic energy of the first mode then grows monotonically without bound. The nonlinear interactions of higher modes are thus necessary in the dynamics of the first mode. However, the isotropic eddy viscosity used in the current closure yields an anisotropic growth rate, though small, among the three normal intensities. To improve the closure with respect to the higher mode-interactions, an alternative approach may be to solve the first and second modes simultaneously and to model the

interactions resulting from the rest of the modes. In that case, the different roles of the first two modes in forming a complete flow should become clear and help answer, in part, the earlier question of the number of modes essential for the flow.

It is briefly mentioned in the last section that the Large Eddy Interaction Model can provide an independent framework to check models for various turbulent processes. The soundness of such a test lies in the fact that the Large Eddy Interaction Model requires a closure assumption for only the nonlinear eddy-eddy interaction terms,and the empirical parameters are chosen on the basis of physical consideration of the large eddies. Now that the first mode is shown to represent the structural character of turbulence, it remains to be determined whether the first two modes are adequate to capture most of the turbulence energy.

APPENDIX A

ALTERNATIVE EXPANSIONS FOR VELOCITY FLUCTUATION

If the instantaneous velocity field is decomposed into a time-mean value and its fluctuation, then

$$\tilde{U}_i = U_1 + u_i \tag{A.1}$$

$$\langle \tilde{U}_i \rangle = U_i \tag{A.2}$$

$$\langle u_i \rangle = 0 \tag{A.3}$$

where $\langle\ \rangle$ denotes a time average. The velocity fluctuation can be expanded in terms of orthonormal functions as opposed to eq. (2).

$$u_i(\vec{x},t) = \sum_{n=1}^{\infty} \alpha_n(t)\phi_1^{(n)}(\vec{x}) \tag{A.4}$$

Notice that the orthonormal functions depend on space. The random coefficients are functions of time and are subject to $\langle \alpha_n(t) \rangle = 0$ by definition. Then the expansion, eq. (A.4), satisfies the premise of eq. (A.3), that is

$$\langle u_i \rangle = \sum_{n=1}^{\infty} \alpha_n(t)\phi_i^{(n)}(\vec{x})$$

$$= \sum_{n=1}^{\infty} \langle \alpha_n(t) \rangle \phi_1^{(n)}(\vec{x})$$

$$= 0 \tag{A.5}$$

Thus, the expansion in eq. (A.4) is consistent with the definition of the velocity fluctuation in eq. (A.3).

Similarly, if U_i in eq. (A.1) is a spatially averaged value, then

$$\{\tilde{U}_i\} = U_1 \tag{A.6}$$

$$\{u_1\} = 0 \tag{A.7}$$

where $\{\ \}$ represents a space average. The velocity fluctuation then can be expanded in the form

$$u_i(\vec{x},t) = \sum_{n=1}^{\infty} \alpha_n(\vec{x})\phi_i^{(n)}(t)$$

with

$$\{\alpha_n(\vec{x})\} = 0 \tag{A.8}$$

so that the expansion in eq. (A.8) satisfies the definition of u_i.

$$\{u_i\} = \left\{\sum_{n=1}^{\infty} \alpha_n(\vec{x})\phi_i^{(n)}(t)\right\}$$

$$= \sum_{n=1}^{\infty} \{\alpha_n(\vec{x})\}\phi_i^{(n)}(t)$$

$$= 0 \tag{A.9}$$

Among the three types of expansions for u_i, which are eqs. (2), (A.4), and (A.8), eq. (2) is the most "fundamental" way of expanding the velocity fluctuations.

APPENDIX B

RELATION BETWEEN VELOCITY SPECTRUM AND SPECTRUM OF TWO-POINT VELOCITY CORRELATION

If mean flow is homogeneous in both streamwise (x) and spanwise (z) coordinates, as is the case of two-dimensional channel flow, one can define spectra of the first mode, $\phi_i^{(1)}$, and of the two-point spatial velocity correlation as follows.

$$\hat{\phi}_i(k_1,y,k_3) = \frac{1}{(2\pi)^2}\iint_{-\infty}^{\infty} \sqrt{\lambda}\phi_i^{(1)}(x,y,z)\exp\{-\hat{i}(k_1x + k_3z)\}dx\,dz \tag{B.1}$$

$$\hat{R}_{ij}(k_1,y,k_3) = \frac{1}{(2\pi)^2}\iint_{-\infty}^{\infty} R_{ij}(r_1,y,r_3)\exp\{-\hat{i}(k_1x + k_3z)\}dx\,dz \tag{B.2}$$

or, inversely,

$$\sqrt{\lambda}\phi_i^{(1)}(x,y,z) = \iint_{-\infty}^{\infty} \hat{\phi}_1(k_1,y,k_3)\exp\{\hat{i}(k_1x + k_3z)\}dk_1\,dk_3 \tag{B.3}$$

$$R_{ij}(r_1,y,r_3) = \iint_{-\infty}^{\infty} \hat{R}_{ij}(k_1,y,k_3)\exp\{\hat{i}(k_1x + k_3z)\}dk_1\,dk_3 \tag{B.4}$$

Here all variables associated with ϕ_i and R_{ij} depend on time implicitly.

Now, consider a product of $\hat{\phi}_i$ and $\hat{\phi}_j$ in the form

$$\hat{\phi}_i(k_1,y,k_3)\hat{\phi}_j(k_1'',y,k_3'')$$

$$= \left\{\frac{1}{(2\pi)^2}\iint_{-\infty}^{\infty} \sqrt{\lambda}\phi_i^{(1)}(x,y,z)\exp[-\hat{i}(k_1x + k_3z)]dx\,dz\right\}$$

$$\times \left\{\frac{1}{(2\pi)^2}\iint_{-\infty}^{\infty} \sqrt{\lambda}\phi_j^{(1)}(x'',y,z'')\exp[-\hat{i}(k_1''x'' + k_3''z'')]dx''\,dz''\right\}$$

$$= \frac{1}{(2\pi)^4}\iiiint_{-\infty}^{\infty} \lambda\phi_i^{(1)}(x,y,z)\phi_j^{(1)}(x'',y,z'')$$

$$\times \exp[-\hat{i}(k_1x + k_3z + k_1''x'' + k_3''z'')]dx\,dz\,dx''\,dz'' \tag{B.5}$$

Let's set x" and z" as

$$x'' = x + r_1 \tag{B.6}$$

$$z'' = z + r_3 \tag{B.7}$$

then

$$\hat{\phi}_i(k_1,y,k_3)\hat{\phi}_j(k_1'',y,k_3'')$$

$$= \frac{1}{(2\pi)^2}\iint_{-\infty}^{\infty}\left\{\frac{1}{(2\pi)^2}\iint_{-\infty}^{\infty}\lambda\phi_i^{(1)}(x,y,z)\phi_j^{(1)}(x'',y,z'')\right.$$

$$\left.\times \exp[-\hat{i}(k_1''r_1 + k_3''r_3)]dr_1\, dr_3\right\}\cdot \exp[-\hat{i}(k_1 + k_1'')x - \hat{i}(k_1 + k_3'')z]dx\, dz \tag{B.8}$$

The integrand in the last expression can be replaced by the two-point velocity correlation, R_{ij}, by way of

$$R_{ij}(r_1,y,r_3) \simeq \lambda^{(1)}\phi_i^{(1)}(x,y,z)\phi_j^{(1)}(x + r_1,y,z + r_3) \tag{B.9}$$

yielding

$$\hat{\phi}_i(k_1,y,k_3)\hat{\phi}_j(k_1'',y,k_3'')$$

$$= \frac{1}{(2\pi)^2}\iint_{-\infty}^{\infty}\left\{\frac{1}{(2\pi)^2}\iint_{-\infty}^{\infty}R_{ij}(r_1,y,r_3)\cdot \exp[-\hat{i}(k_1''r_1 + k_3''r_3)]dr_1\, dr_3\right\}$$

$$\times \exp\left[-\hat{i}[(k_1 + k_1'')x + (k_3 + k_3'')z]\right]dx\, dz$$

$$= \frac{1}{(2\pi)^2}R_{ij}(k_1'',y,k_3'')\iint_{-\infty}^{\infty}\exp\{-\hat{i}[(k_1 + k_1'')x + (k_3 + k_3'')z]\}dx\, dz \tag{B.10}$$

Fourier transform of a constant is then the Dirac delta function, that is

$$\delta(\vec{k} + \vec{k}'') = \frac{1}{(2\pi)^2}\iint_{-\infty}^{\infty}\exp\{-\hat{i}[(k_1 + k_1'')x + (k_3 + k_3'')z]\}dx\, dz \tag{B.11}$$

or

$$1 = \iint_{-\infty}^{\infty}\delta(\vec{k} + \vec{k}'')\exp\{(\vec{k} + \vec{k}'')\cdot\vec{x}\}d(\vec{k} + \vec{k}'')$$

By substituting eq. (B.11) into eq. (B.10), one arrives at

$$\hat{\phi}_i(k_1,y,k_3)\hat{\phi}_j(k_1'',y,k_3'') = \hat{R}_{ij}(k_1'',y,k_3'')\delta(\vec{k} + \vec{k}'')$$

or

$$\hat{R}_{ij}(-k_1,y,-k_3) = \hat{\phi}_i(k_1,y,k_3)\hat{\phi}_j(-k_1,y,-k_3) \tag{B.12}$$

which is given in eq. (24) and leads subsequently to the following via eqs. (25) and (26).

$$\overline{u_i u_j}(y) = \iint_{-\infty}^{\infty} \hat{\phi}_i(k_1,y,k_3)\hat{\phi}_j(-k_1,y,-k_3)dk_1\, dk_3 \tag{B.13}$$

Here one can utilize the following symmetry condition implied in eqs. (B.3) and (B.4) for the integration.

$$\hat{\phi}_i(k_1,y,k_3) = \hat{\phi}_i^*(-k_1,y,-k_3)$$

$$\hat{\phi}_i(-k_1,y,k_3) = \hat{\phi}_i^*(k_1,y,-k_3)$$

$$\hat{R}_{ij}(k_1,y,k_3) = R_{ij}^*(-k_1,y,-k_3)$$

That is, the real parts of $\hat{\phi}_i$ and $\hat{R}_{ij}$ are even functions, and the imaginary parts are odd functions with respect to the wave number, $\vec{k}$.

Another way of obtaining $\overline{u_i u_j}(y)$ may be to (a) calculate $\phi_i^{(1)}(x,y,z)$ and $\phi_j^{(1)}(x,y,z)$ separately from eq. (B.1), (b) multiply them directly in the (x,z)-plane for $\phi_i^{(1)}\phi_j^{(1)}$, and (c) take a spatial average over a period which the product would possess in both x- and z-coordinates. Thus, the alternative will be more tedious than the analytical methods in the above, eq. (B.13), and the solution depends on the averaging technique which is unnecessary in the spectral method.

REFERENCES

Bakewell, H. P.; and Lumley, J. L.: Viscous Sublayer and Adjacent Wall Region in Turbulent Pipe Flow. Phys. Fluids, vol. 10, 1967, pp. 1880-1889.

Blackwelder, R. F.; and Eckelmann, H.: Streamwise Vortices Associated with the Bursting Phenomenon. J. Fluid Mech., vol. 94, 1979, pp. 577-594.

Cebeci, T.; and Smith, A. M. O.: Analysis of Turbulent Boundary Layers. Academic Press, New York, 1974.

Comte-Bellot, G.: Contribution a l'éude de la turbulence de conduite. Ph.D. Thesis, Univ. of Grenoble, 1963.

Deissler, R. G.: Turbulent Solutions of the Equations of Fluid Motion. Reviews of Modern Physics, vol. 56, no. 2, April 1984, pp. 223-254.

Glushko, G. S.: Turbulent Boundary Layer on a Flat Plate in an Incompressible Fluid. Bull. Acad. Sci., USSR, Mech. Ser. 4, 1965, pp. 13-23.

Goldstein, S.: Modern Developments in Fluid Dynamics. Oxford Univ. Press, London, 1950, p. 357.

Greenspan, D.: Discrete Numerical Methods in Physics and Engineering. Academic Press, New York, 1974, pp. 130-140.

Hanjalic, K.; and Launder, B. E.: A Reynolds Stress Model of Turbulence and Its Application to Thin Shear Flows. J. Fluid Mech., vol. 52, part 4, 1972, pp. 609-638.

Hinze, J. O.: Turbulence. McGraw-Hill, New York, 1975, chap. 7.

Hong, S. K.: Large Eddy Interactions in Curved Wall Boundary Layers--Model and Implications. Ph.D. Thesis, Purdue Univ., 1983.

Hong, S. K.; and Murthy, S. N. B.: Structure of Turbulence in Curved Wall Boundary Layers. AIAA Paper 83-0457, Jan. 1983.

Hong, S. K.; and Murthy, S. N. B.: On Effective Velocity of Transport in Curved Wall Boundary Layers. AIAA Paper 84-0177, Jan. 1984a. Also to be published in AIAA J.

Hong, S. K.; and Murthy, S. N. B.: Pressure-Strain Correlations in Curved Wall Boundary Layers. AIAA Paper 84-1671, June 1984b. Also to be published in AIAA J.

Jones, W. P.; and Launder, B. E.: The Prediction of Laminarization with a Two-Equation Model of Turbulence. Int. J. Heat Mass Transfer, vol. 15, 1972, pp. 301-314.

Kreplin, H.-P.; and Eckelmann, H.: Behavior of the Three Fluctuating Velocity Components in the Wall Region of a Turbulent Channel Flow. Phys. Fluids, vol. 22, July 1979, pp. 1233-1239.

Laufer, J.: Investigation of Turbulent Flow in a Two-dimensional Channel. NACA Rep. 1053, 1951.

Lemmerman, L. A.; and Payne, F. R.: Extraction of the Large Eddy Structure of a Turbulent Boundary Layer. AIAA Paper 77-717, June 1977.

Loeve, M.: Probability Theory. Second ed., D. Van Nostrand Co., 1960, pp. 477-480.

Lumley, J. L.: The Structure of Inhomogeneous Flows. Atmospheric Turbulence and Radio Wave Propagation, A. M. Yaglom and V. I. Tartarsky, eds., Publishing House <<NAUKA>>, Moscow, 1967, pp. 166-176.

Lumley, J. L.: Coherent Structures in Turbulence. Transition and Turbulence, R. E. Meyer, ed., Academic Press, New York, 1981, pp. 215-242.

Lumley, J. L.; and Panofsky, H. A.: The Structure of Atmospheric Turbulence, Interscience Pub., 1964, Appendix B.

Mellor, G. L.; and Herring, H. J.: A Survey of the Mean Turbulent Field Closure Models. AIAA J., vol. 11, no. 5, May 1973, pp. 590-599.

Moin, P.: Probing Turbulence via Large Eddy Simulation. AIAA Paper 84-0174, Jan. 1984.

Moin, P.; and Kim, J.: Numerical Investigation of Turbulent Channel Flow. vol. 118, 1982, pp. 341-377.

Moin, P.; Reynolds, W. C.; and Ferziger, J. H.: Large Eddy Simulation of Incompressible Turbulent Channel Flow. Technical Report No. TF-12, Dept. of Mech. Eng., Stanford University, 1978.

Murphy, J. D.; and Rubesin, M. W.: A Navier-Stokes Fast Solver for Turbulent Modeling Applications. NASA TM-78612, Aug. 1979.

Payne, F. R.; and Lumley, J. L.: Large Eddy Structure of the Turbulent Wake Behind a Circular Cylinder. Phys. Fluids, vol. 10, 1967, pp. S194-S196.

Pearson, J. R. A.: The Effect of Uniform Distortion on Weak Homogeneous Turbulence. J. Fluid Mech., vol. 5, 1959, pp. 274-288.

Saffman, P. G.: A Model for Inhomogeneous Turbulent Flows. Proc. Roy. Soc., London, vol. A317, no. 1530, 1970, pp. 417-433.

Tolstov, G. P.: Fourier Series. Dover Publications, New York, 1962, chap. 2.

Townsend, A. A.: The Structure of Turbulent Shear Flow. First ed., Cambridge Univ. Press, London, 1956, pp. 107-110, 247.

Townsend, A. A.: The Structure of Turbulent Shear Flow. Second ed., Cambridge Univ. Press, London, 1976, chap. 3, pp. 295-298.

Townsend, A. A.: The Response of Sheared Turbulence to Additional Distortion. J. Fluid Mech., vol. 81, part 1, 1980, pp. 171-191.

Willmarth, W. W.; and Tu, B. J.: Structure of Turbulence in the Boundary Layer near the Wall. Phys. Fluids, vol. 10, 1967, pp. S134-S137.

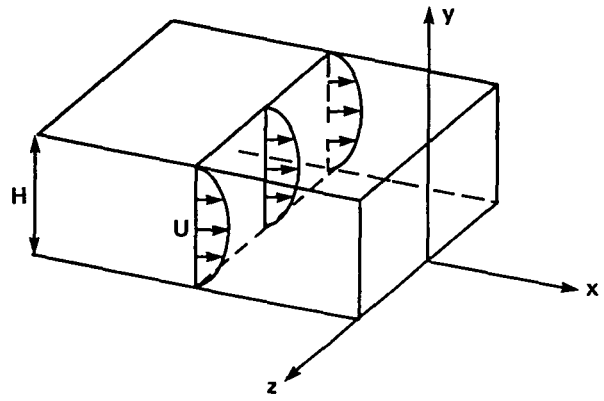

Figure 1.- Coordinate system for a two-dimensional channel flow.

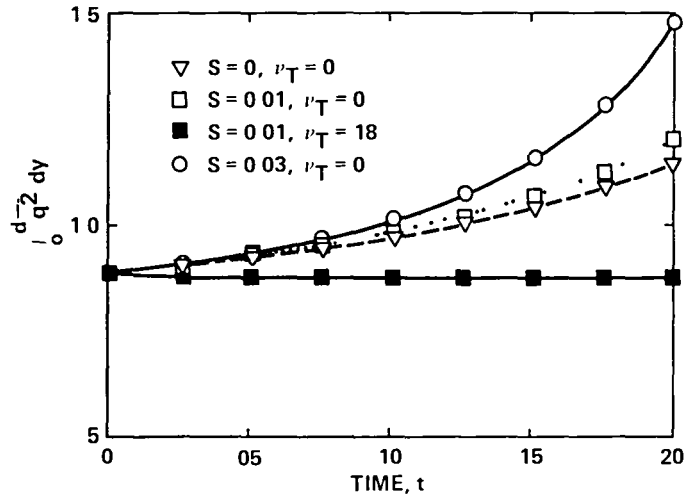

Figure 2.- Turbulent kinetic energy vs $\tilde{t}$ (= tU_0/H) for various values of skewness parameter, S.

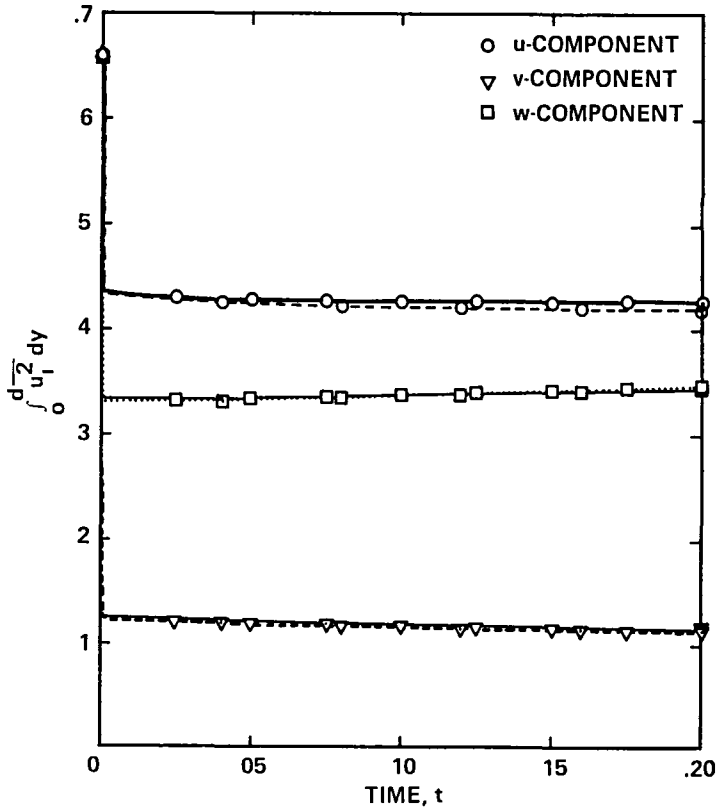

Figure 3.- Turbulent energy growth in time among three components for two sets of parameters: solid line for (S = 0.01, ν_t = 18); dashed line for (S = 0.03, ν_T = 22)..

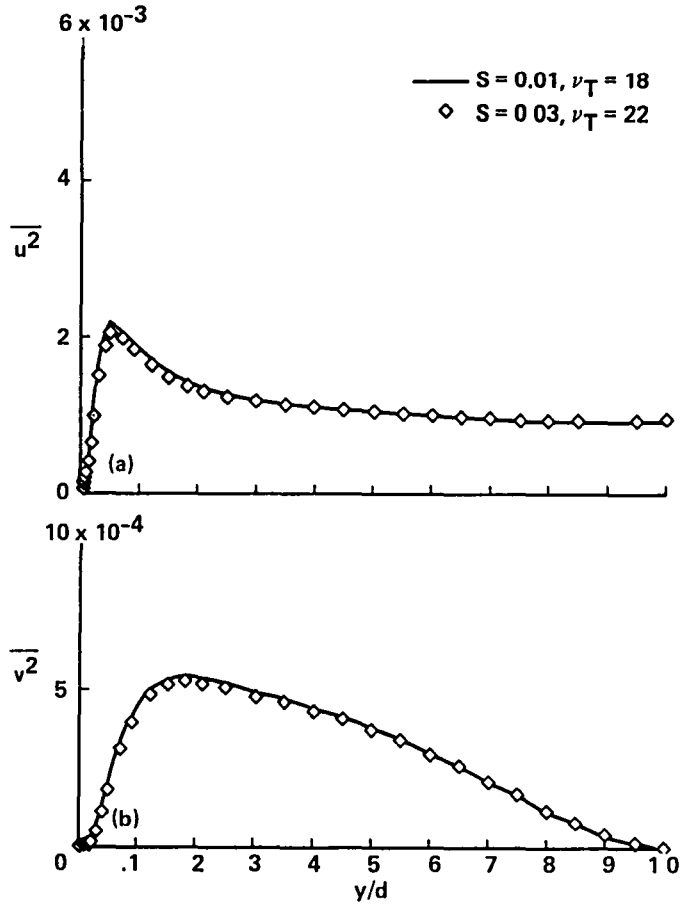

Figure 4.- Comparison of Reynolds stresses calculated, based on two sets of parameters: $S = 0.01$ and $\nu_t = 18$ (solid line); $S = 0.03$ and $\nu_T = 22$ (◇◇◇).

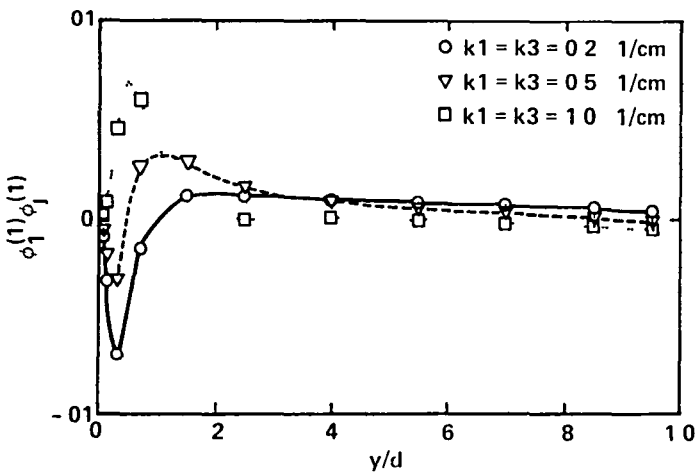

Figure 5.- Profiles of $S(\partial/\partial x_j)\{\tilde{\phi}_1^{(1)})(\tilde{\phi}_j^{(1)})\}$ versus y/d for various wave numbers at $\tilde{t} = 0.2$.

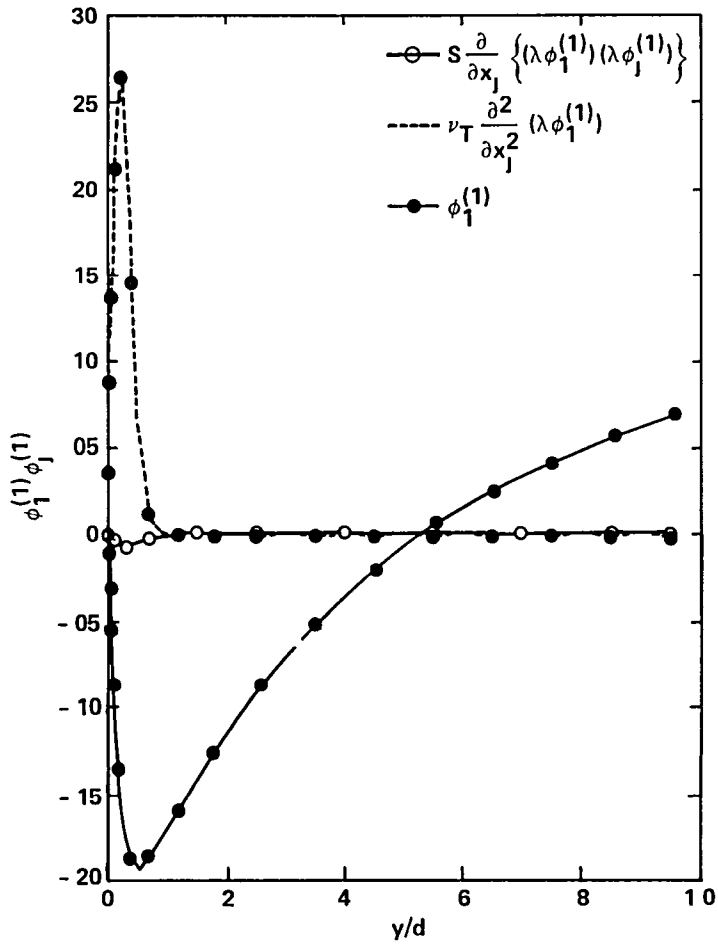

Figure 6(a).- Profiles of large eddy self-interactions and modeled higher mode interactions versus y/d for k_1 = 0.1 and k_3 = 0.05 (1/cm) at $\tilde{t}$ = 0.2.

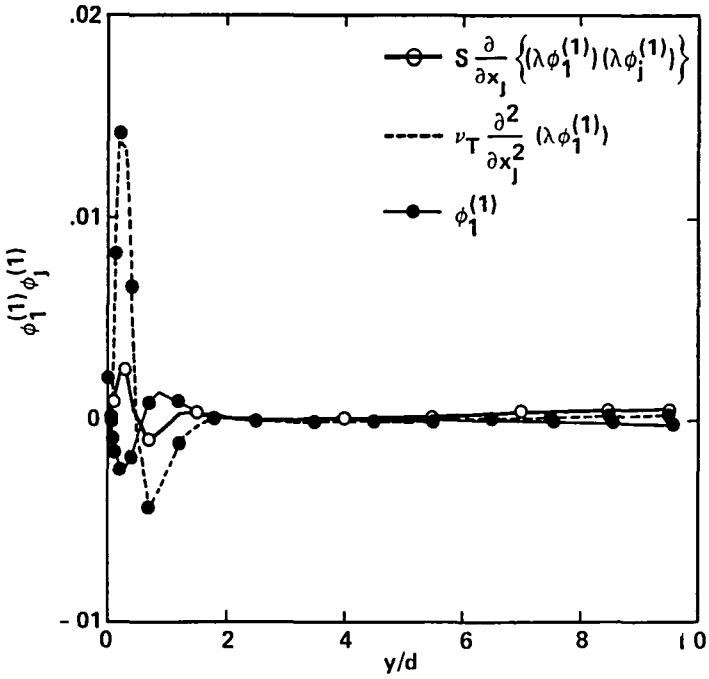

Figure 6(b).- Profiles of large eddy self-interactions and modeled higher mode interactions versus y/d for k_1 = 5.0 and k_3 = 0.05 (1/cm) at $\tilde{t}$ = 0.2.

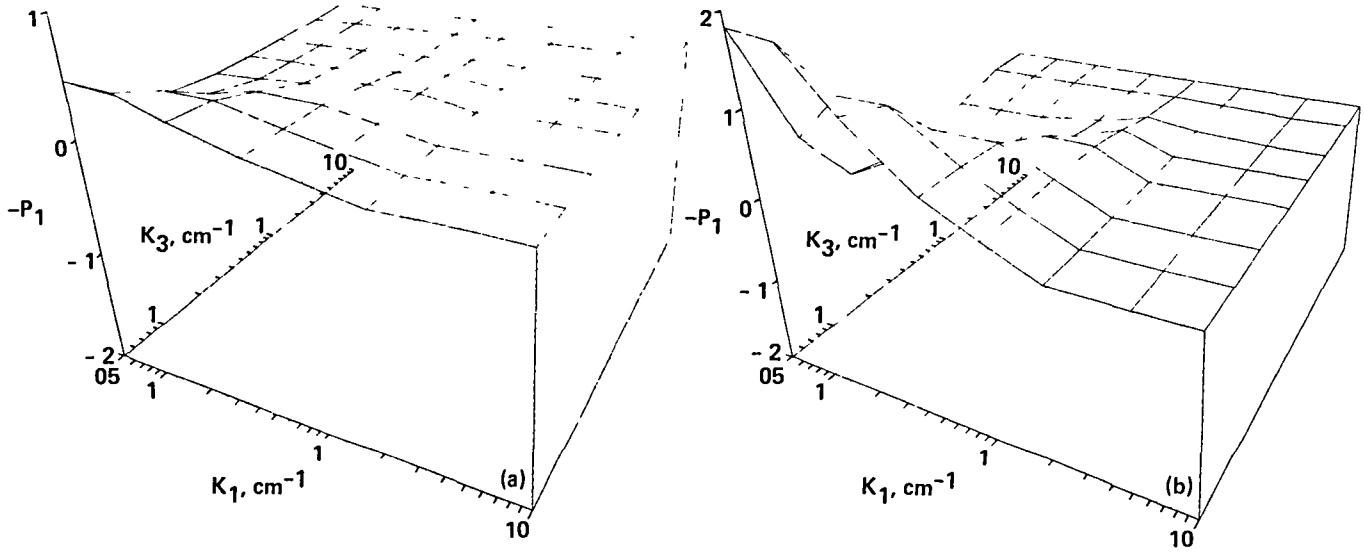

Figure 7.- Distribution of P_1 in the (k_1,k_3)-space at (a) y^+ = 7 and (b) y/d = 0.09. $\tilde{t}$ = 0.2.

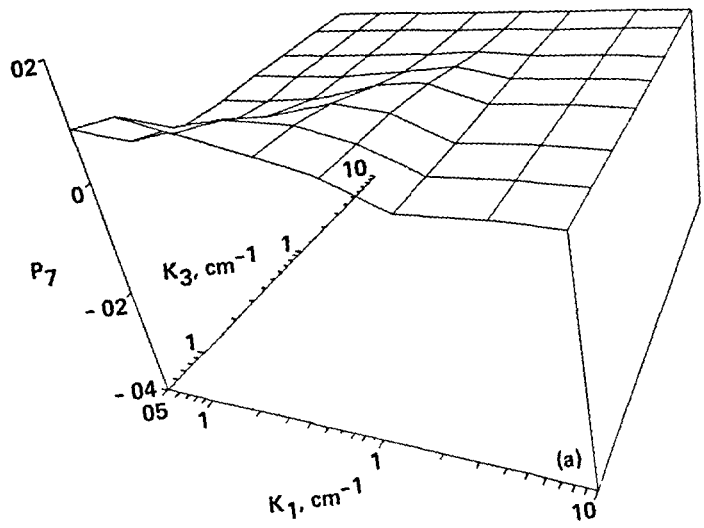

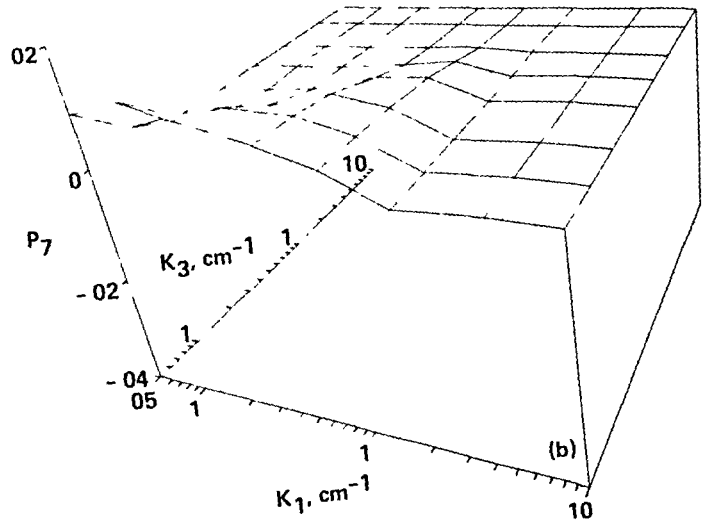

Figure 8.- Distribution of P_7 in the (k_1,k_3)-space at (a) $y^+ = 7$ and (b) $y/d = 0.09$. $\tilde{t} = 0.2$.

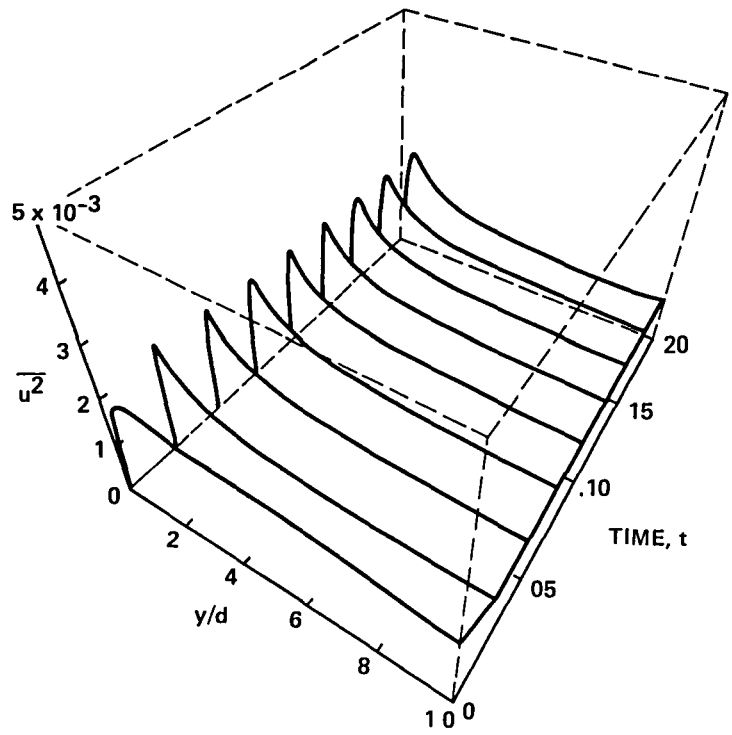

Figure 9.- Development of streamwise turbulent intensity ($\overline{u^2}/U_o^2$) in (y,t).

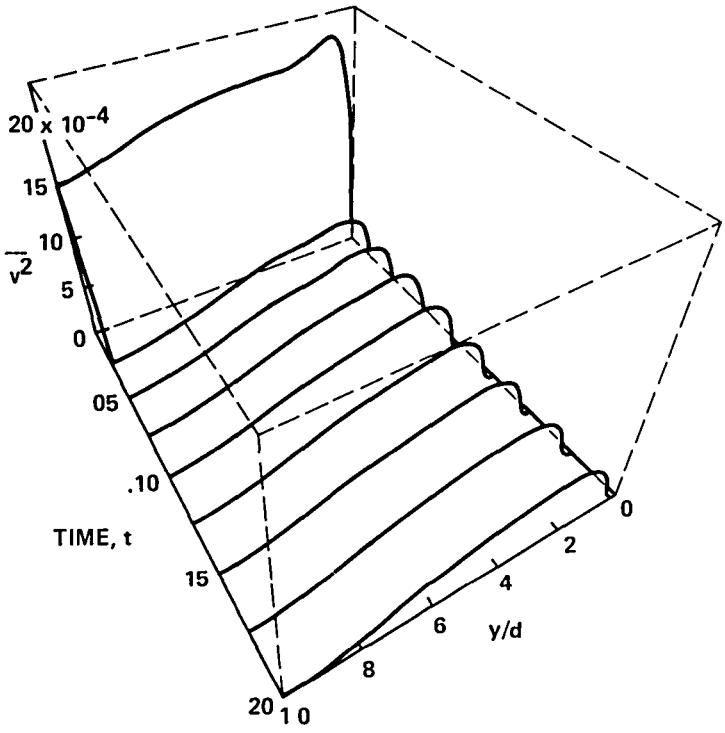

Figure 10.- Development of normal turbulent intensity (v^2/U_o^2) in (y,t) space.

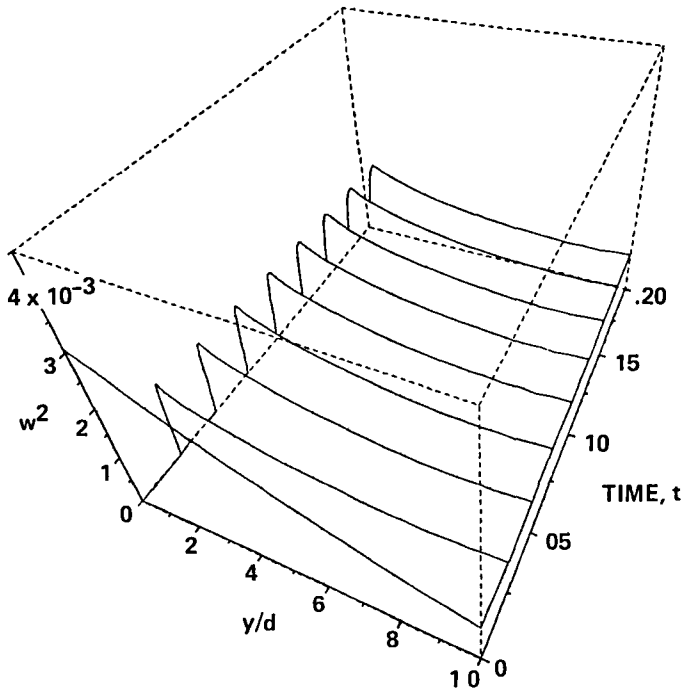

Figure 11.- Development of spanwise turbulent intensity ($\overline{w^2}/U_o^2$) in the (y,t)-space.

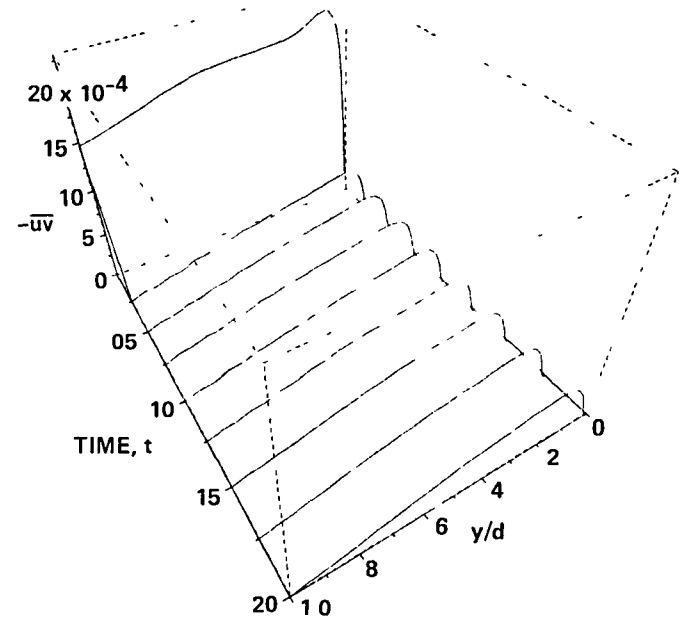

Figure 12.- Development of shear stress ($\overline{uv}/U_o^2$) in the (y,t)-space.

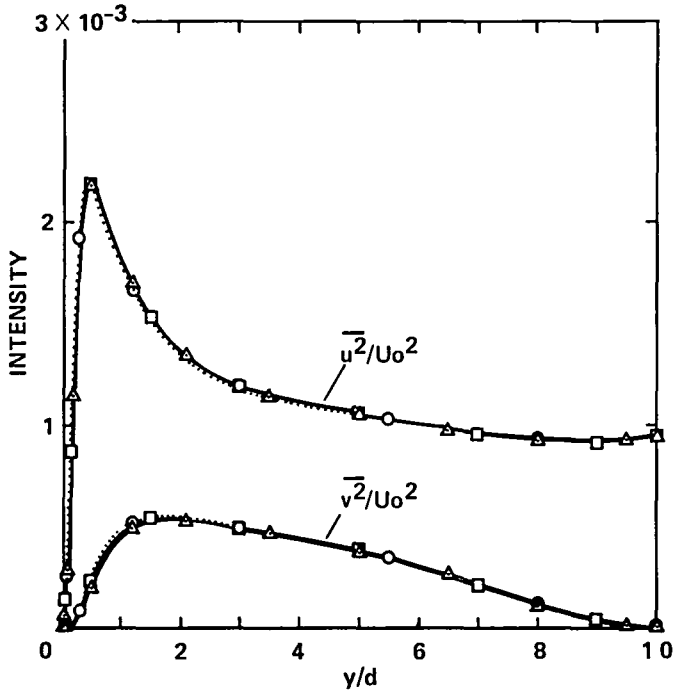

Figure 13.- Comparison of three $\overline{u^2}$ and $\overline{v^2}$ profiles at $t = 0.15$ (o), 0.175 (×), and 0.2 (△).

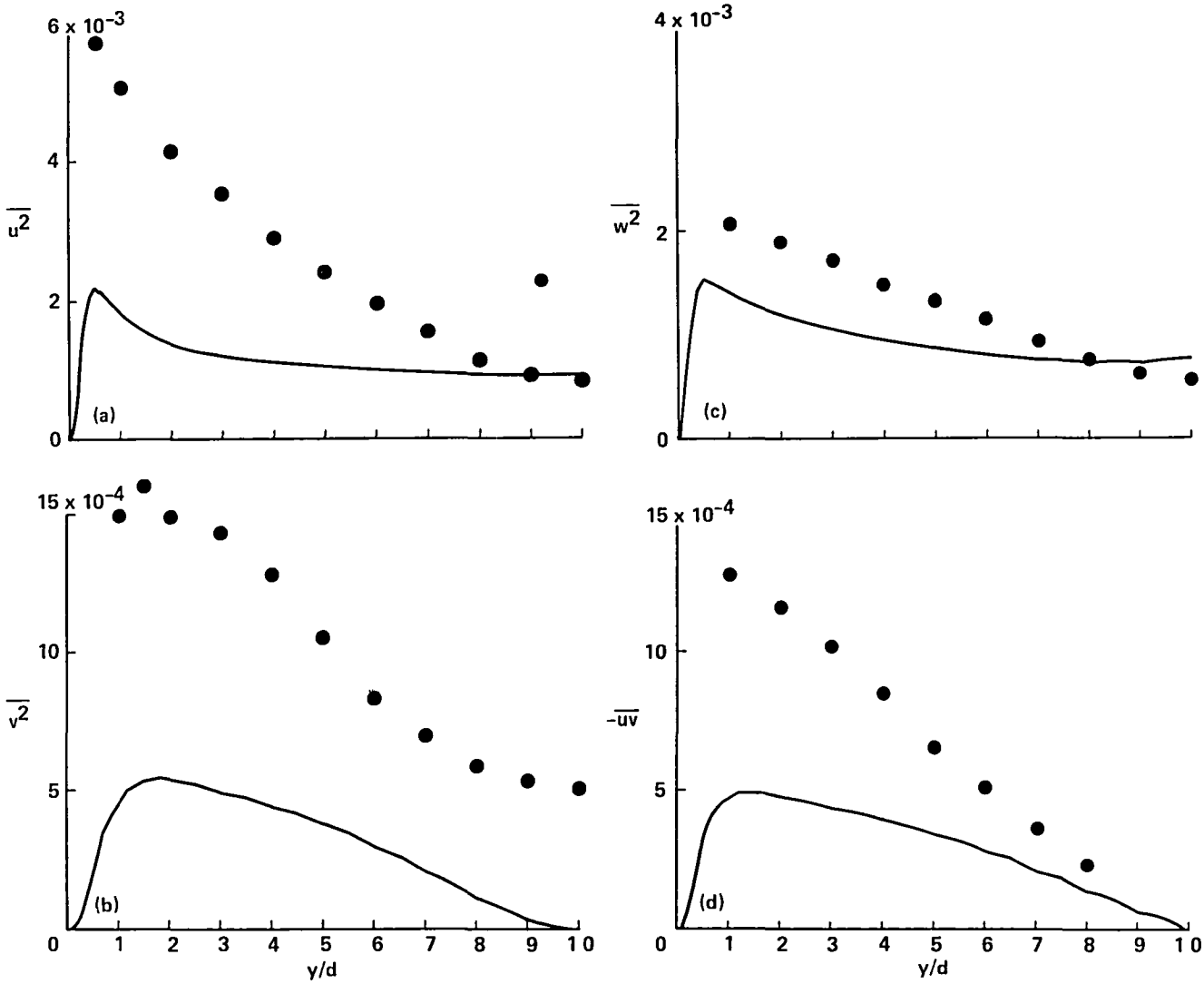

Figure 14.- Contribution from the first mode to (a) $\overline{u^2}$, (b) $\overline{v^2}$, (c) $\overline{w^2}$, and (d) $\overline{uv}$, divided by U_o^2, versus y/d at t = 0.2: •• Laufer (1951).

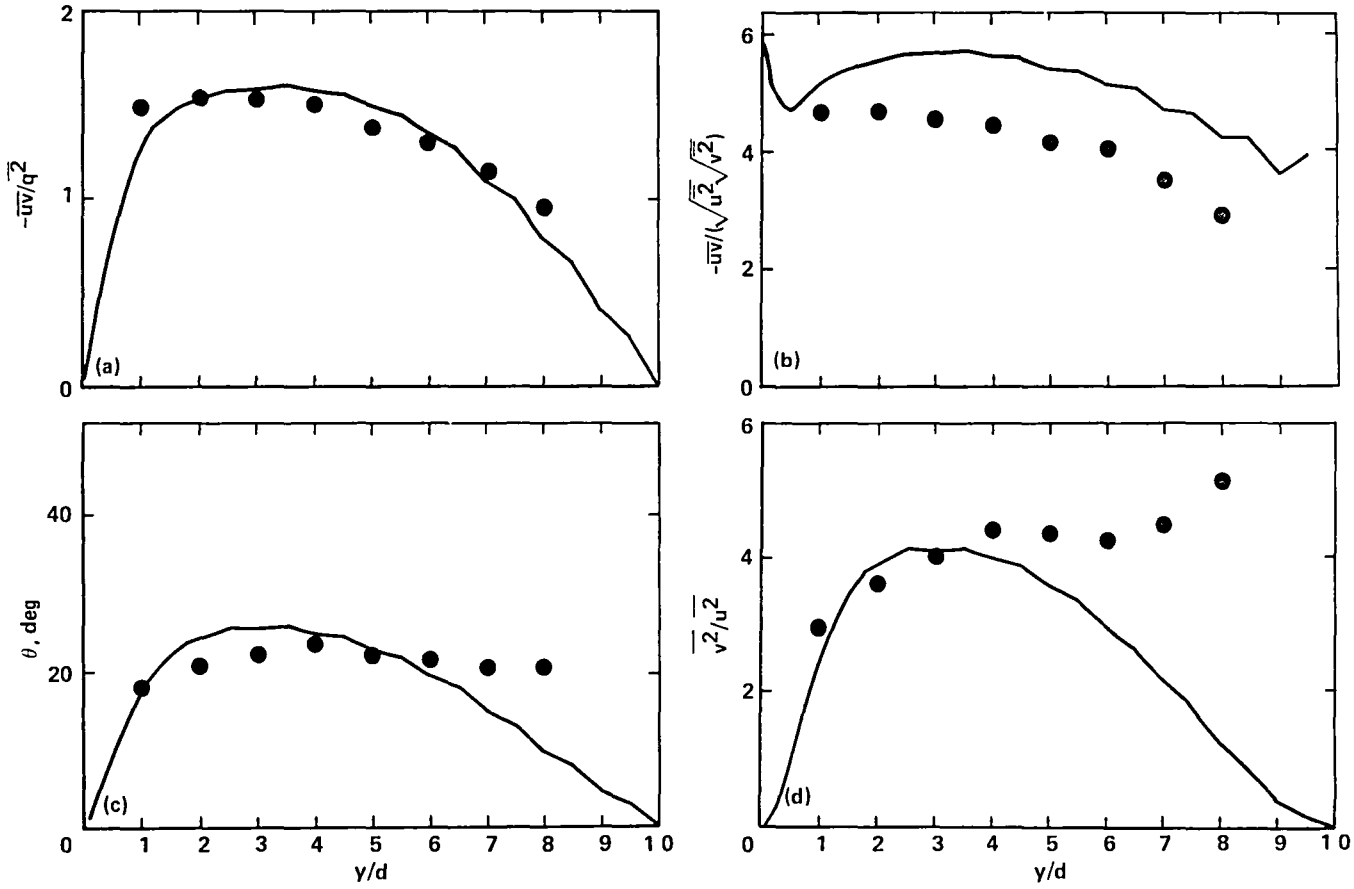

Figure 15.- Structural quantities calculated from the first mode versus y/d at t = 0.2: •• Laufer (1951); (a) $\overline{uv}/\overline{q^2}$, (b) $\overline{uv}/\sqrt{\overline{u^2}}\sqrt{\overline{v^2}}$, (c) θ in equation (28), and (d) $\overline{v^2}/\overline{u^2}$.

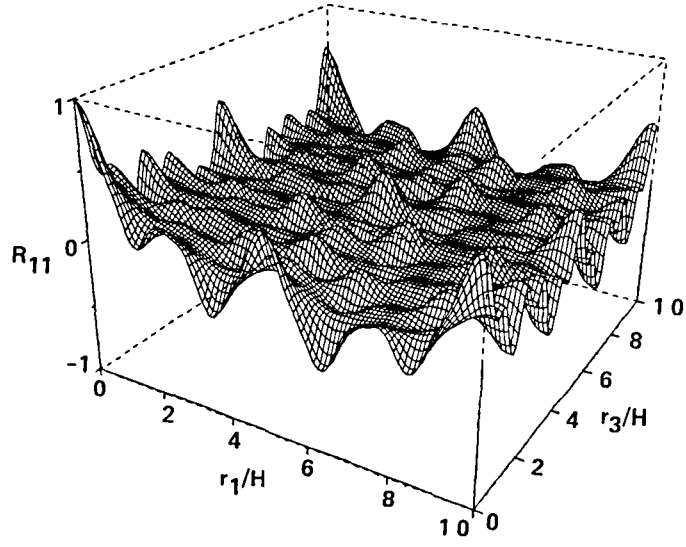

Figure 16.- Two-point velocity correlation, R_{11} obtained from eq. (25), as a function of (r_1, r_3) at $y^+ = 7$.

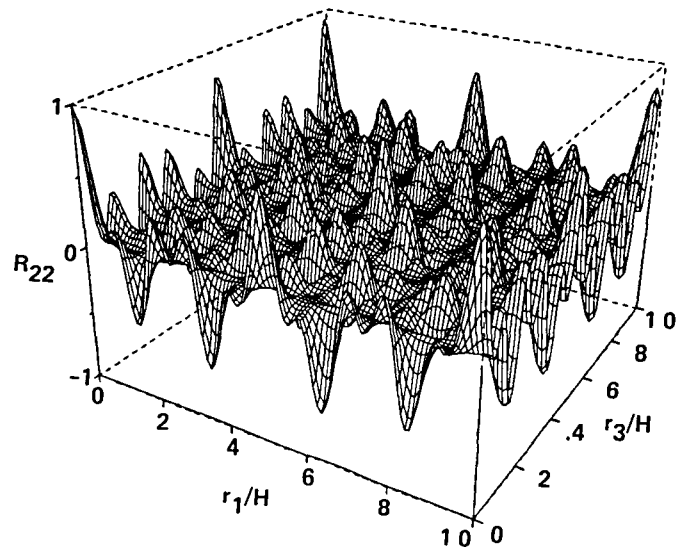

Figure 17.- Two-point velocity correlation, R_{22} obtained from eq. (25), as a function of (r_1,r_3) at $y^+ = 7$.

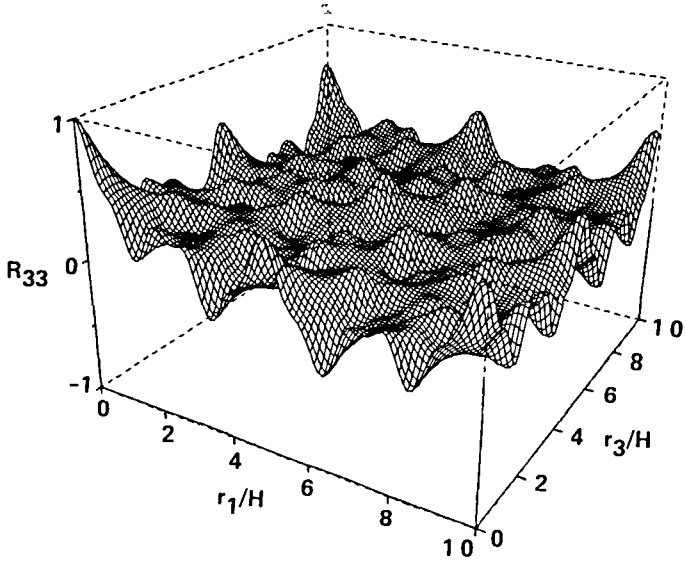

Figure 18.- Two-point velocity correlation, R_{33} obtained from eq. (25), as a function of (r_1,r_3) at $y^+ = 7$.

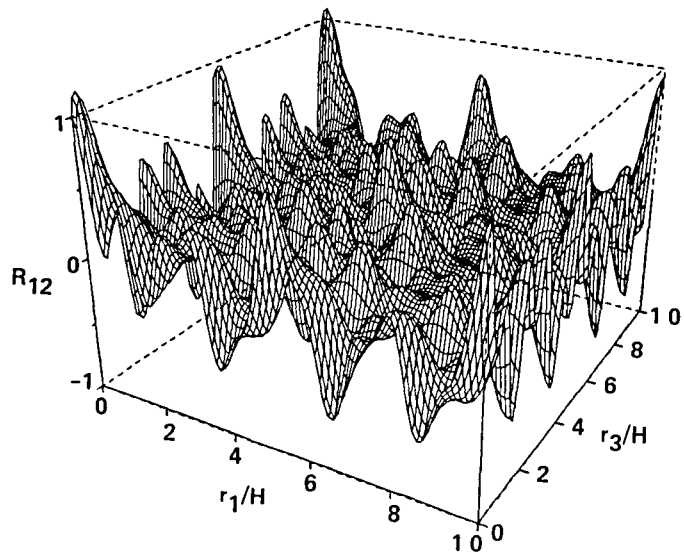

Figure 19.- Two-point velocity correlation, R_{12} obtained from eq. (25), as a function of (r_1, r_3) at $y^+ = 7$.

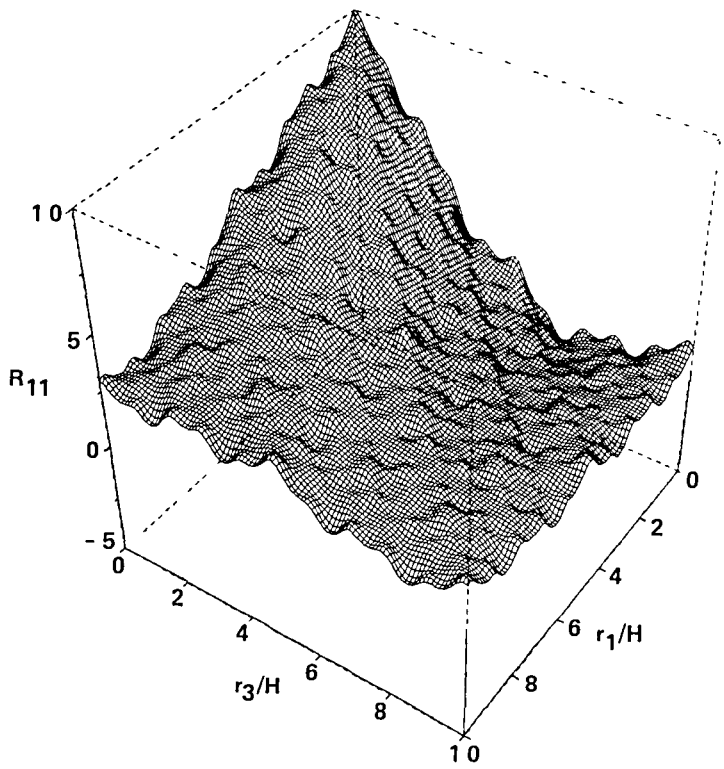

Figure 20.- Two-point velocity correlation, R_{11} obtained from eq. (25), as a function of (r_1, r_3) at $y/d = 0.5$.

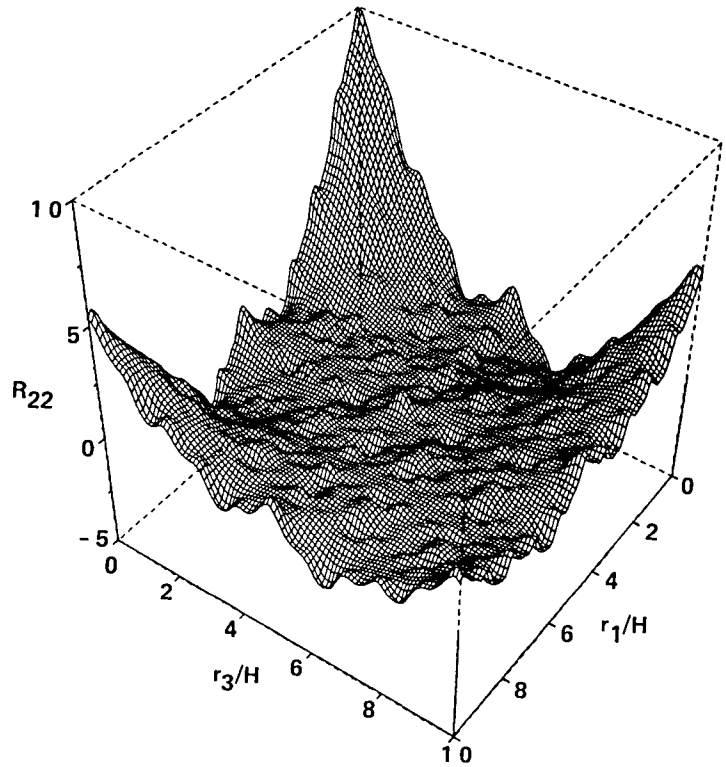

Figure 21.- Two-point velocity correlation, R_{22} obtained from eq. (25), as a function of (r_1,r_3) at y/d = 0.5.

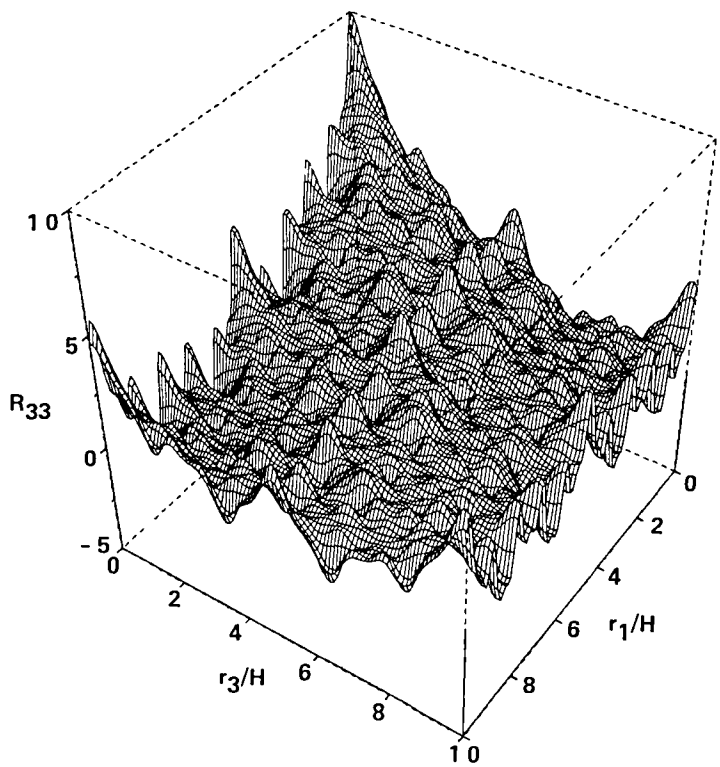

Figure 22.- Two-point velocity correlation, R_{33} obtained from eq. (25), as a function of (r_1,r_3) at y/d = 0.5.

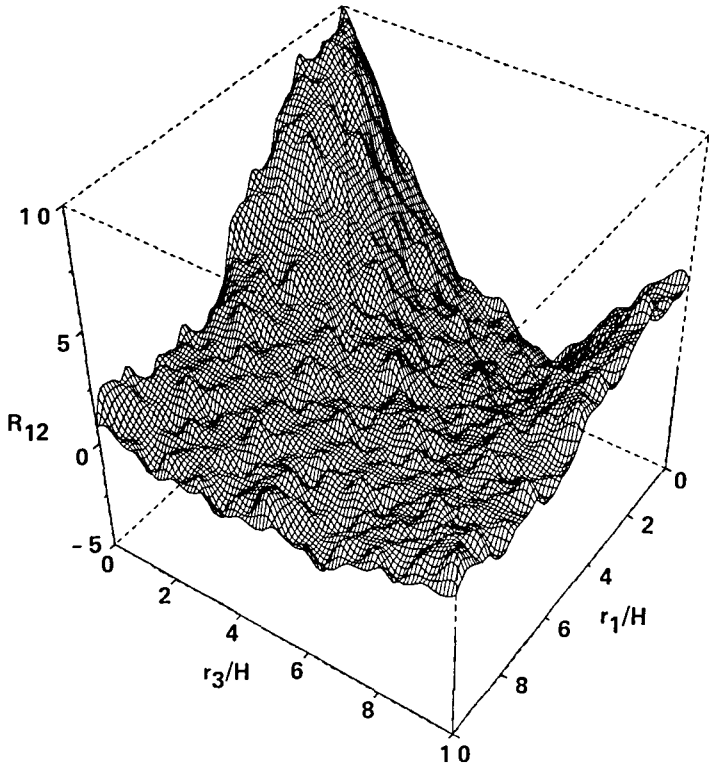

Figure 23.- Two-point velocity correlation, R_{12} obtained from eq. (25), as a function of (r_1, r_3) at $y/d = 0.5$.

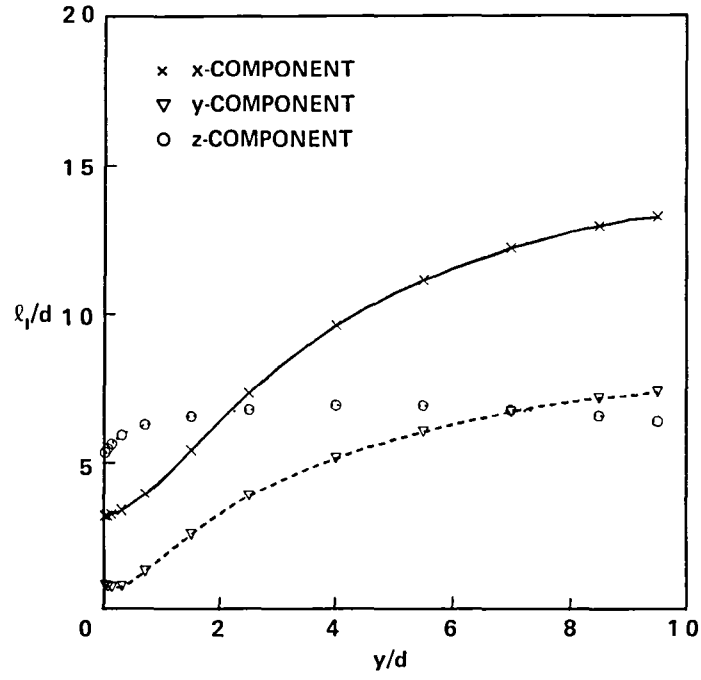

Figure 24.- Integral length scale of large eddy defined by eq. (34) vs. y/d.

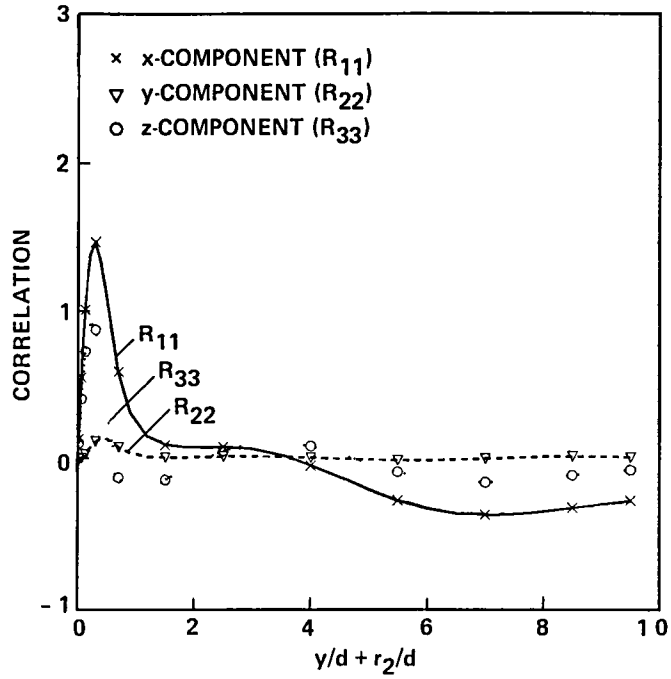

Figure 25.- Two-point velocity correlations obtained from eq. (35) as a function of r_2 at $y^+ = 7$.

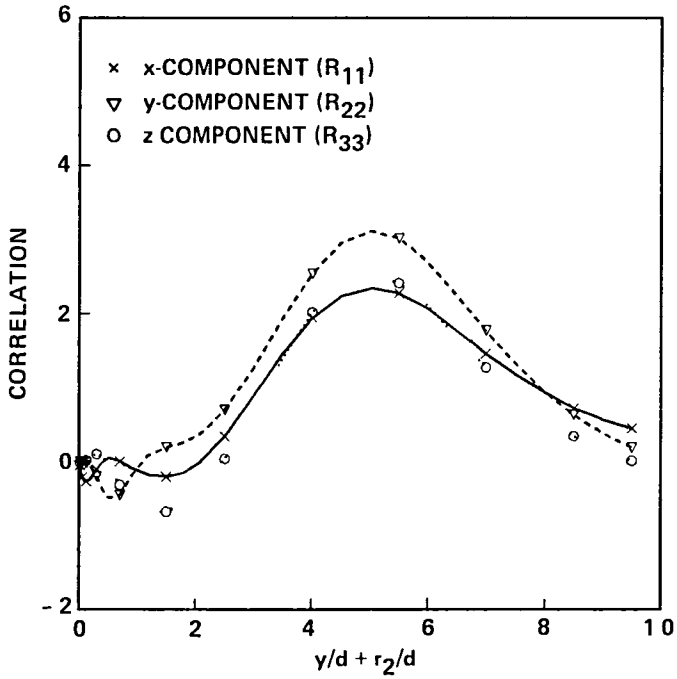

Figure 26.- Two-point velocity correlations obtained from eq. (35) as a function of r_2 at $y/d = 0.5$.

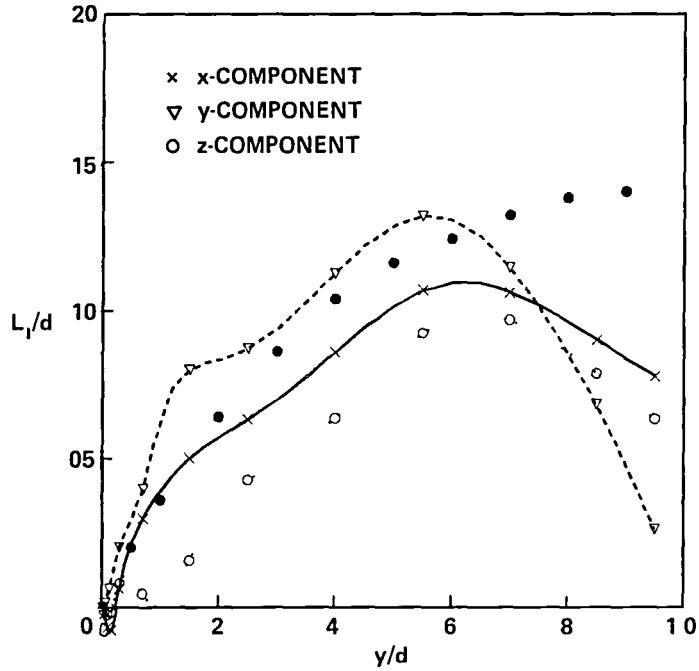

Figure 27.- Integral length scale of large eddy defined by eq. (36) vs. y/d: •• Goldstein (1950).

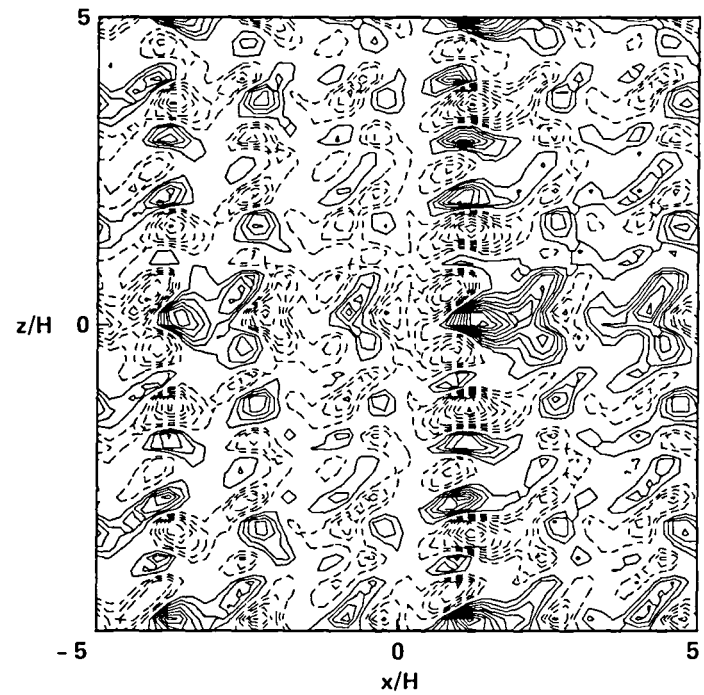

Figure 28.- Contour plot of $u^{(1)}$ in the (x,z)-plane at $y^+ = 7$.

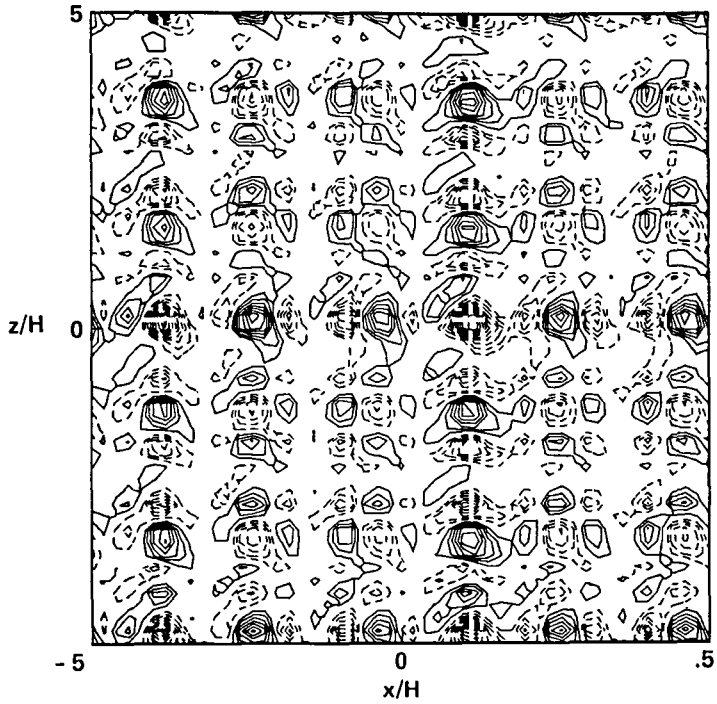

Figure 29.- Contour plot of $v^{(1)}$ in the (x,z)-plane at $y^+ = 7$.

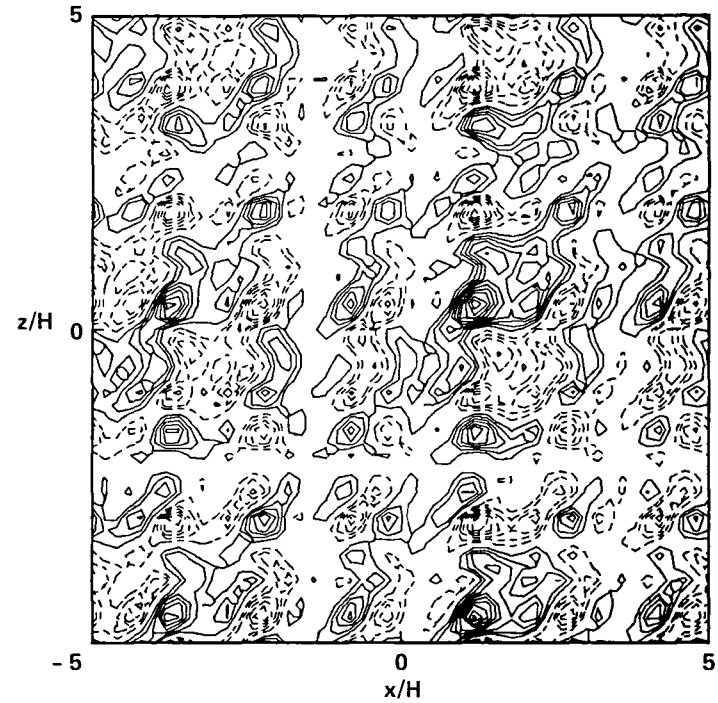

Figure 30.- Contour plot of $w^{(1)}$ in the (x,z)-plane at $y^+ = 7$.

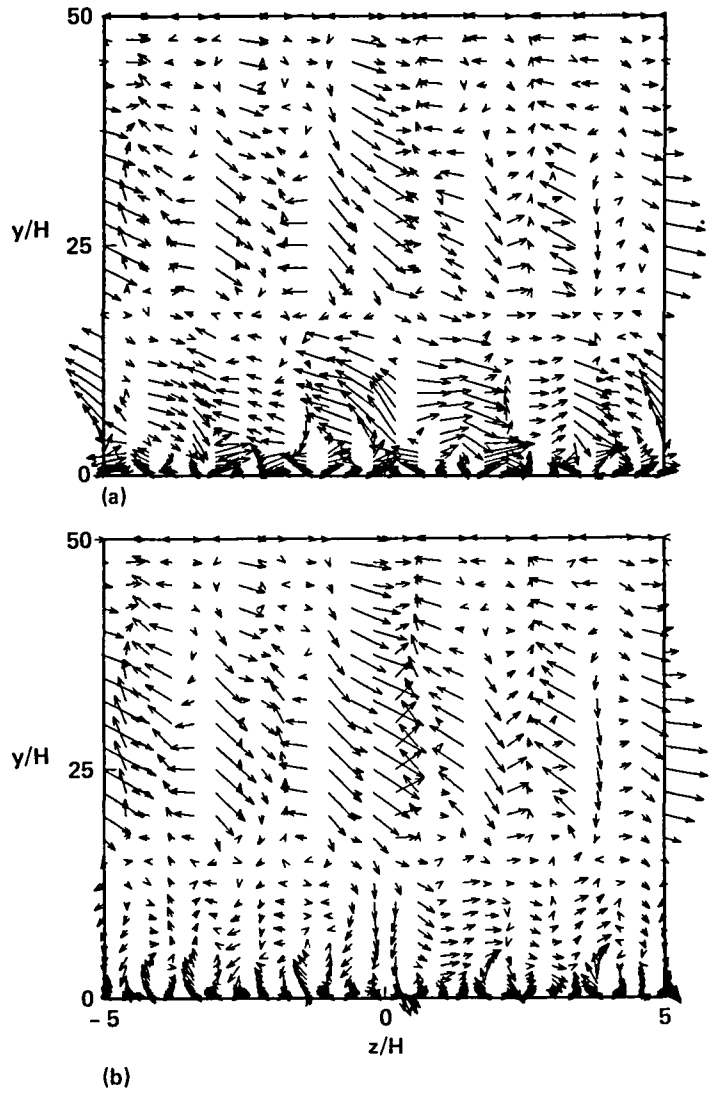

Figure 31.- Velocity vector of large eddy in the (y,z)-plane at (a) x/H = 0.3 and (b) x/H = 0.4.

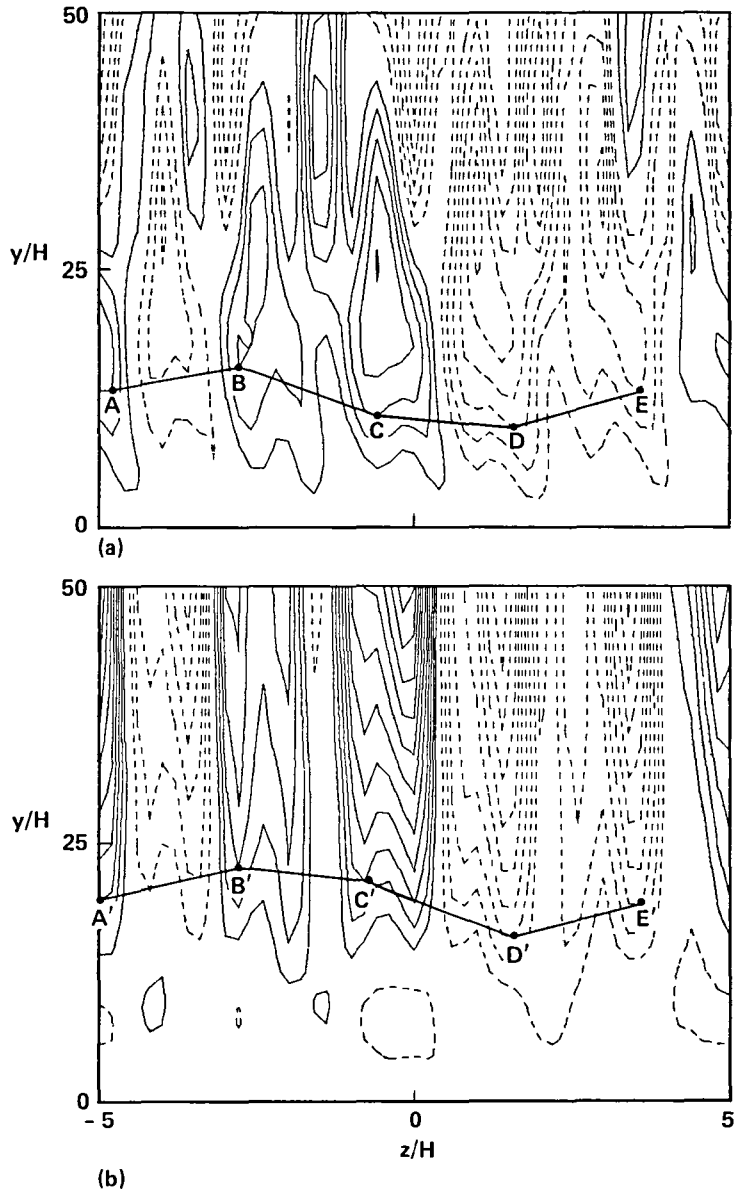

Figure 32.- Stream function contours in the (y,z)-plane at (a) x/H = 0.3 and (b) x/H = 0.34.

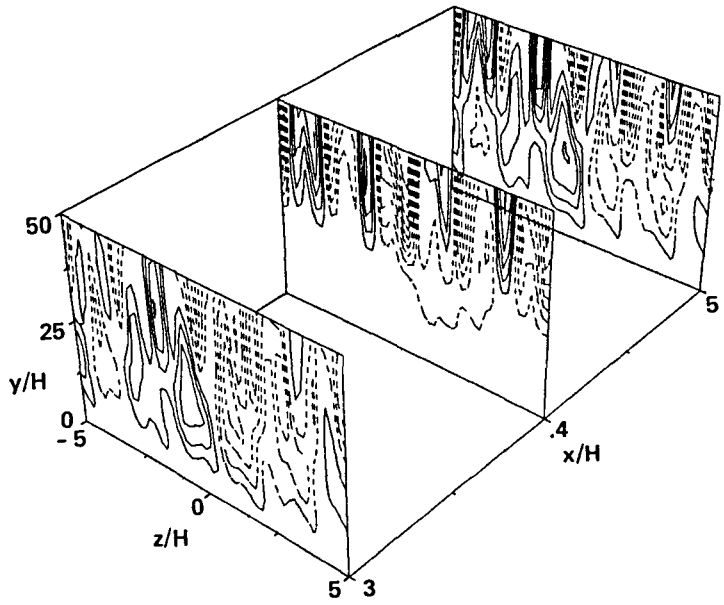

Figure 33.- Stream function ψ_1 (eq. (39)) contours in the (y,z)-plane at x/H = 0.3, 0.4, and 0.5.

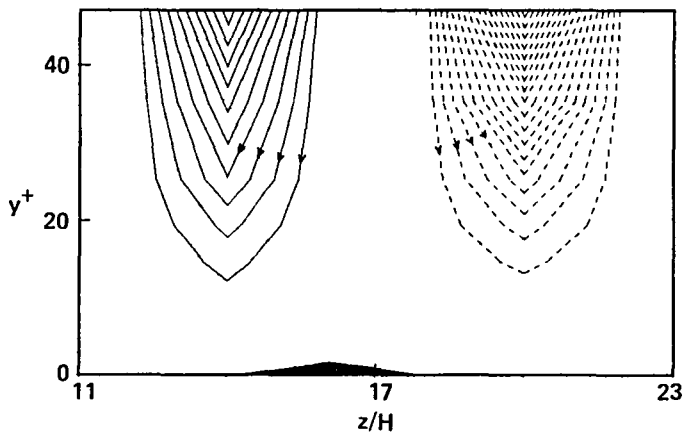

Figure 34.- Stream function ψ_1 contours in the (y,z)-plane in the viscous region.

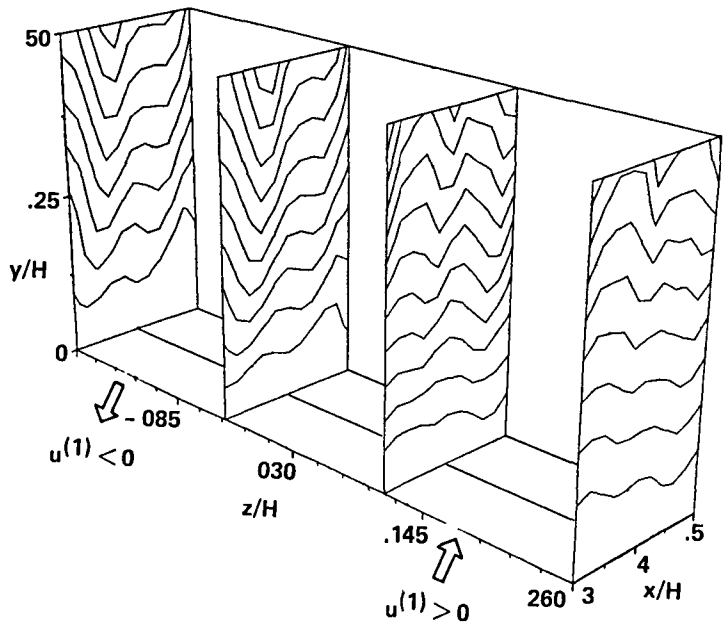

Figure 35.- Stream function ψ_2 (eq. (40)) contours in the (x,y)-plane at four locations of z.

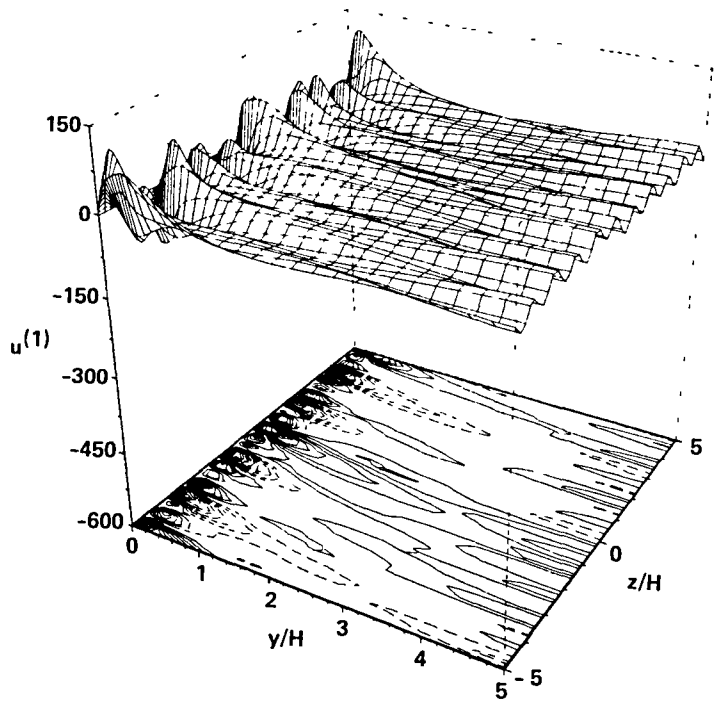

Figure 36.- Large eddy velocity fluctuation, $u^{(1)}$, in the (y,z)-plane at x/H = 0.12.

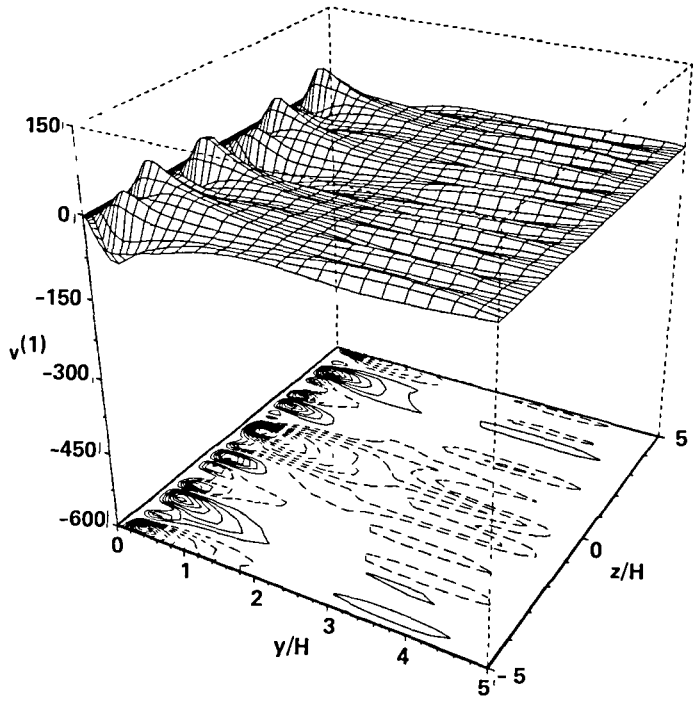

Figure 37.- Large eddy velocity fluctuation, $v^{(1)}$, in the (y,z)-plane at x/H = 0.12.

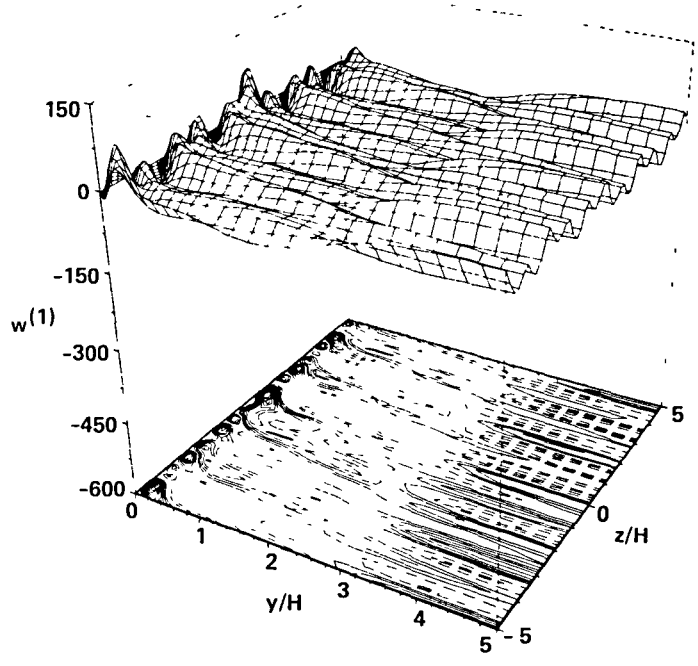

Figure 38.- Large eddy velocity fluctuation, $w^{(1)}$, in the (y,z)-plane at x/H = 0.12.

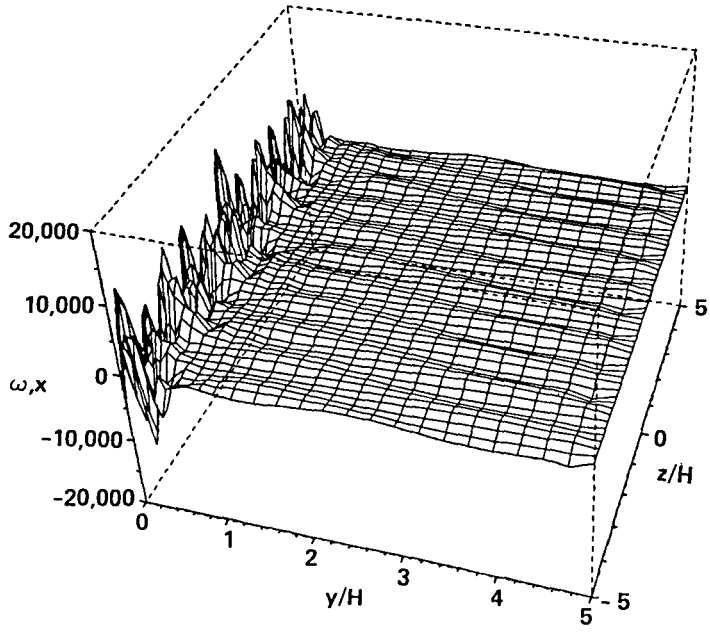

Figure 39.- Streamwise vorticity fluctuation of large eddy in the (y,z)-plane at x/H = 0.12.

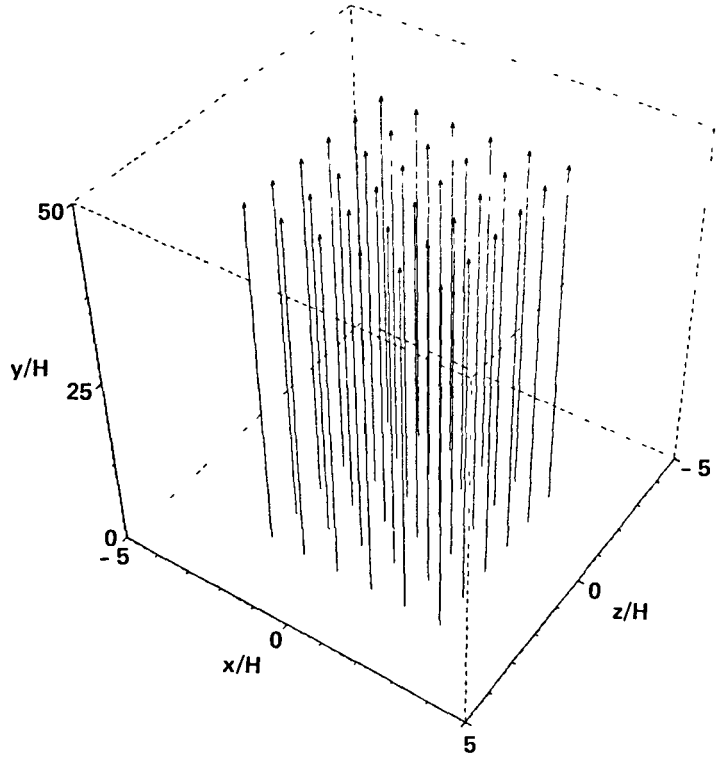

Figure 40.- A volume of the flow represented by 36 lines in the physical space.

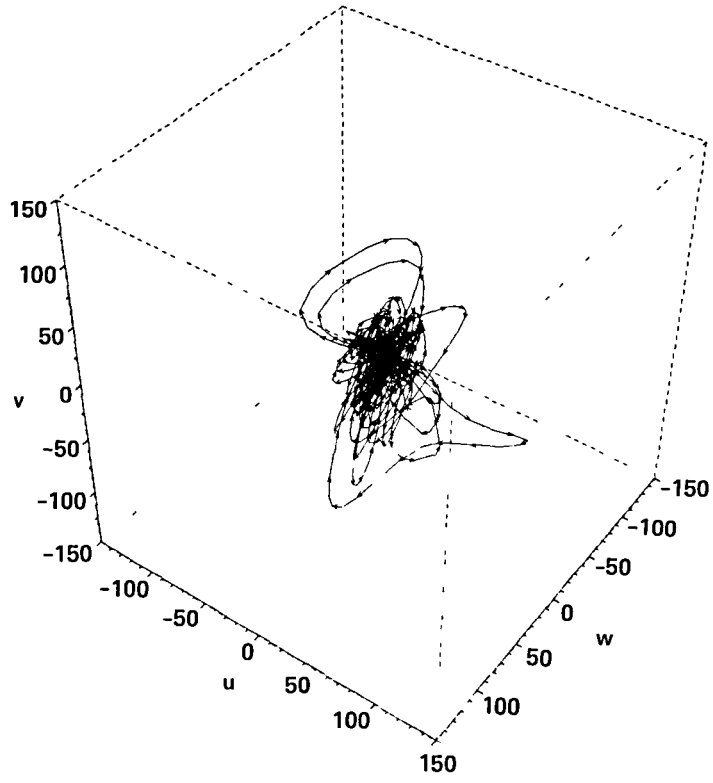

Figure 41.- Traces of velocities along the lines shown in figure 40 at $\tilde{t} = 0.2$.

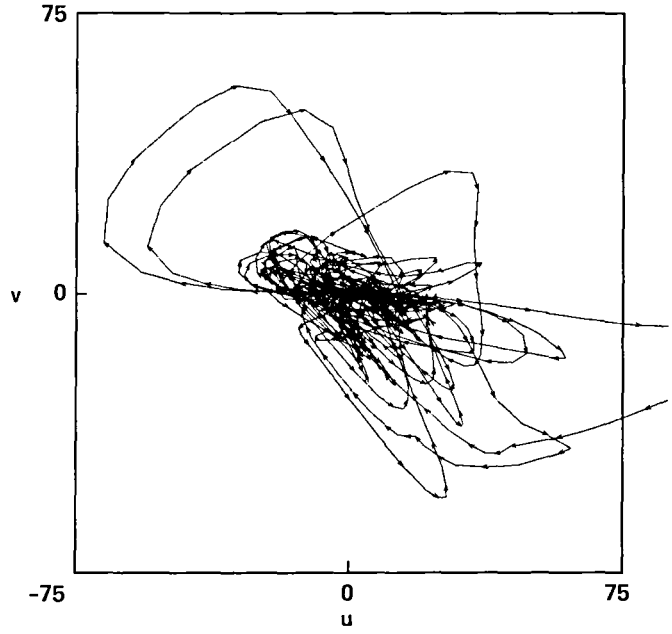

Figure 42.- Projection of velocity traces in figure 41 onto the (u,v)-plane, at $\tilde{t} = 0.2$.

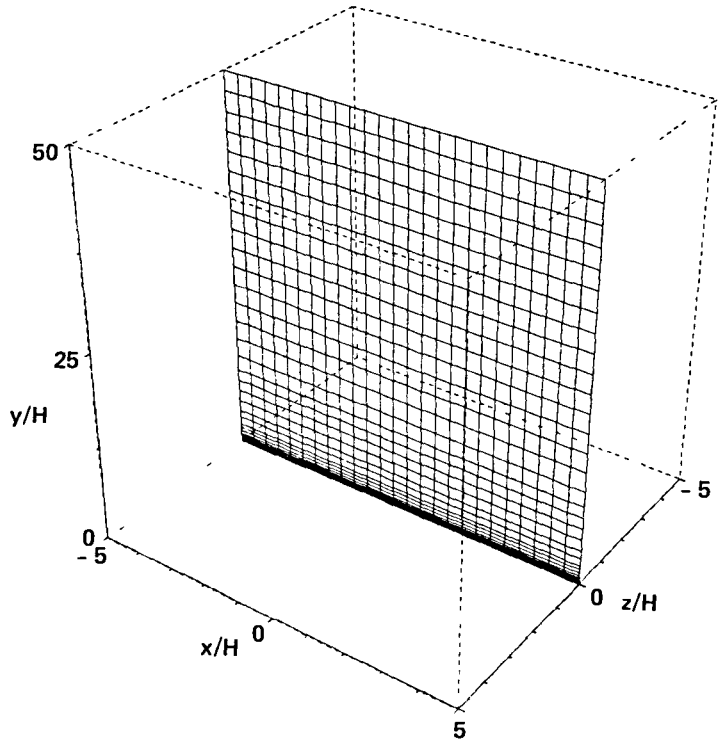

Figure 43.- A plane in the physical space at $z = 0$.

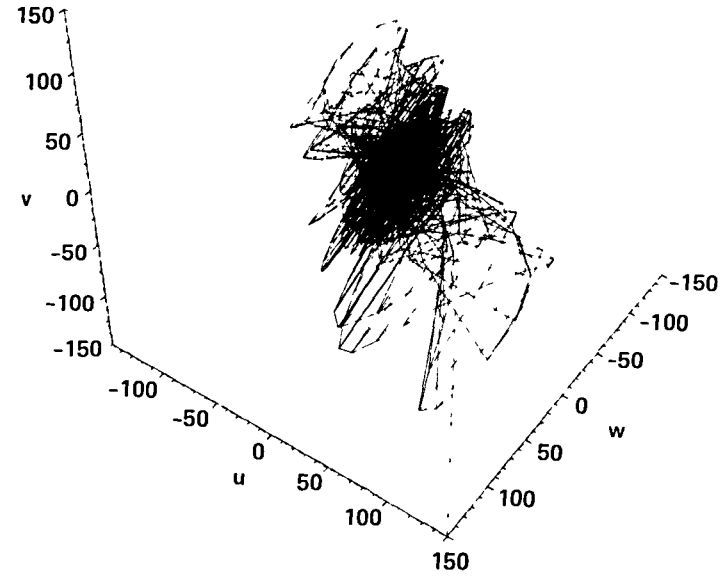

Figure 44.- Traces of velocities taken from every grid point in figure 43, at $\tilde{t} = 0.2$.

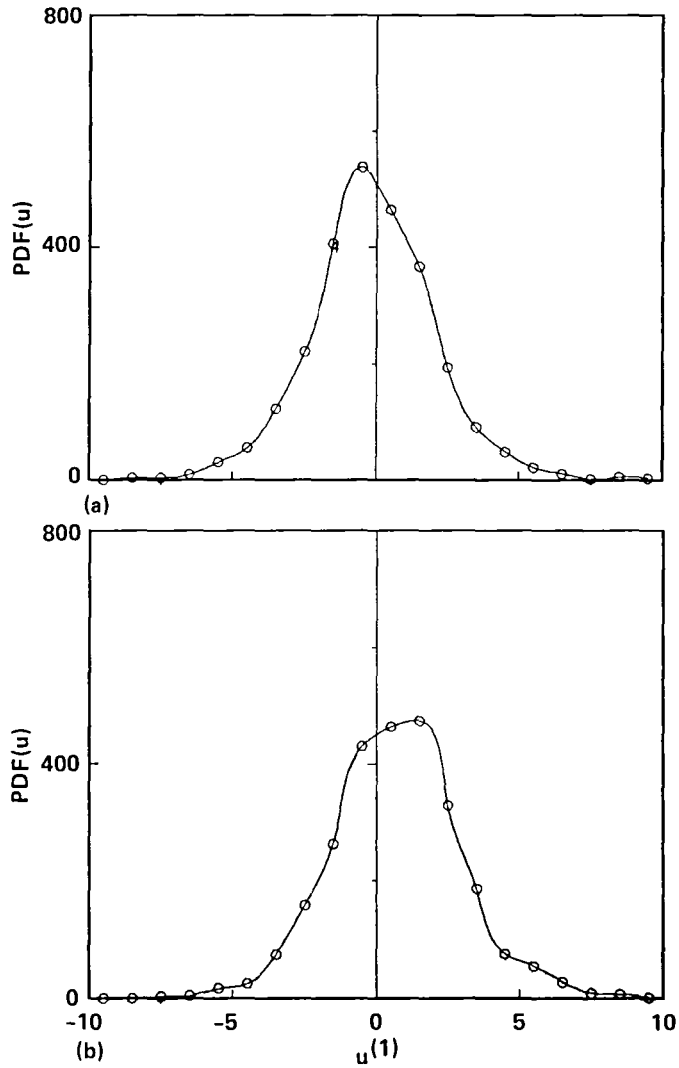

Figure 45.- Probability distribution function of the u-component of a large eddy in the homogeneous space: (a) $y^+ = 7$, (b) $y/d = 0.5$.

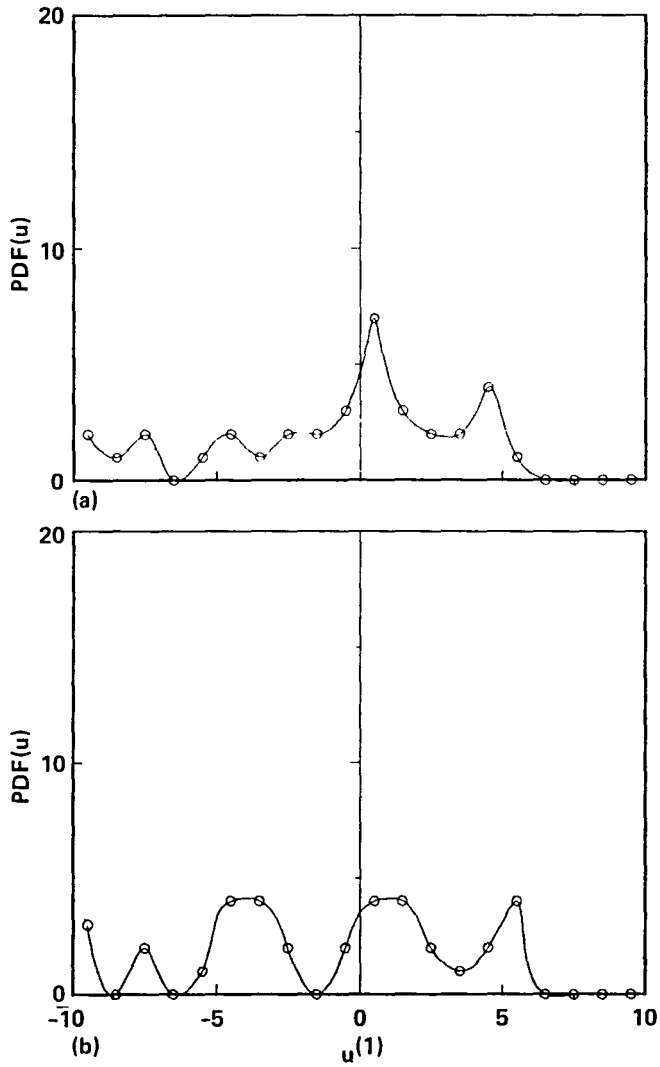

Figure 46.- Probability distribution function of the u-component of a large eddy along y at (a) x = z = 0 and (b) x = z = 0.1H.

1 Report No	2 Government Accession No	3 Recipient's Catalog No
NASA TM-86757		

4 Title and Subtitle	5 Report Date
LARGE EDDY INTERACTIONS IN A TURBULENT CHANNEL FLOW	September 1985
	6 Performing Organization Code
7 Author(s)	8 Performing Organization Report No
S. K. Hong, NRC Research Associate	85265
	10 Work Unit No
9 Performing Organization Name and Address	11 Contract or Grant No
Ames Research Center Moffett Field, CA 94035	
	13 Type of Report and Period Covered
12 Sponsoring Agency Name and Address	Technical Memorandum
National Aeronautics and Space Administration Washington, DC 20546	14 Sponsoring Agency Code 505-31-01

15 Supplementary Notes

Point of Contact: S. K. Hong, Ames Research Center, MS 229-1, Moffett Field, CA 94035 (415) 694-6229 or FTS 464-6229

16 Abstract

The dynamic processes of large eddies in a turbulent channel flow have been examined by utilizing an orthogonal expansion of the velocity fluctuation, known in the literature as the Proper Orthogonal Decomposition Theorem. The mathematical form of these functions is unknown, in contrast to the Fourier analysis. Attention is focused on the nonlinear, turbulence-turbulence interaction process in the dynamical equation for large eddies (the first term in the expansion). The nonlinear interactions of the components of the first mode are treated exactly, but influences of higher modes are modeled. This requires adjustment of both the skewness and the effective Reynolds number so that the energy equilibrium of the large eddies is ensured when the mean velocity distribution is assumed known from experiments. Computational results show that the first mode contributes significantly to turbulent intensities and possesses a structural and statistical character similar to that of the entire flow.

17 Key Words (Suggested by Author(s))

Large eddy
Proper orthogonal expansion
Channel flow
Reynolds stress
Turbulence structure

18 Distribution Statement

Unlimited

Subject Category - 34

19 Security Classif (of this report)	20 Security Classif (of this page)	21 No of Pages	22 Price*
Unclassified	Unclassified	65	A04

*For sale by the National Technical Information Service, Springfield, Virginia 22161

End of Document